DRAFT VERSION JULY 25, 2020
Typeset using LATEX **twocolumn** style in AASTeX63

Cluster Difference Imaging Photometric Survey (CDIPS) II. TOI 837: A Young Validated Planet in IC 2602

L. G. BOUMA,[1] J. D. HARTMAN,[1] R. BRAHM,[2,3] P. EVANS,[4] K. A. COLLINS,[5] G. ZHOU,[5] P. SARKIS,[6] S. N. QUINN,[5] J. DE LEON,[7] J. LIVINGSTON,[7] C. BERGMANN,[8] K. G. STASSUN,[9,10] W. BHATTI,[1] J. N. WINN,[1] G. Á. BAKOS,[1] L. ABE,[11] A. AGABI,[11] N. CROUZET,[12] G. DRANSFIELD,[13] T. GUILLOT,[11] W. MARIE-SAINTE,[14] D. MÉKARNIA,[11] A. H.M.J. TRIAUD,[13] C. G. TINNEY,[8,15] T. HENNING,[6] N. ESPINOZA,[16] A. JORDÁN,[2,3] M. BARBIERI,[17] S. NANDAKUMAR,[17] T. TRIFONOV,[6] J. I. VINES,[18] M. VUCKOVIC,[19] C. ZIEGLER,[20] C. BRICEÑO,[21] N. LAW,[22] A. W. MANN,[22] G. R. RICKER,[23] R. VANDERSPEK,[23] D. W. LATHAM,[5] S. SEAGER,[24] J. M. JENKINS,[25] C. J. BURKE,[23] D. DRAGOMIR,[26] C. X. HUANG,[23] R. C. KIDWELL, JR.,[27] A. M. LEVINE,[23] E. QUINTANA,[28] J. E. RODRIGUEZ,[5] J. C. SMITH,[25,29] AND B. WOHLER[25,29]

[1]*Department of Astrophysical Sciences, Princeton University, 4 Ivy Lane, Princeton, NJ 08540, USA*
[2]*Facultad de Ingeniería y Ciencias, Universidad Adolfo Ibáñez, Av. Diagonal las Torres 2640, Peñalolén, Santiago, Chile*
[3]*Millennium Institute for Astrophysics, Chile*
[4]*El Sauce Observatory, Coquimbo Province, Chile*
[5]*Center for Astrophysics | Harvard & Smithsonian, 60 Garden St, Cambridge, MA 02138, USA*
[6]*Max-Planck-Institut für Astronomie, Königstuhl 17, Heidelberg 69117, Germany*
[7]*Department of Astronomy, University of Tokyo, 7-3-1 Hongo, Bunkyo-ky, Tokyo 113-0033, Japan*
[8]*Exoplanetary Science at UNSW, School of Physics, UNSW Sydney, NSW 2052, Australia*
[9]*Vanderbilt University, Department of Physics & Astronomy, 6301 Stevenson Center Lane, Nashville, TN 37235, USA*
[10]*Fisk University, Department of Physics, 1000 17th Avenue N., Nashville, TN 37208, USA*
[11]*Université Côte d'Azur, Observatoire de la Côte d'Azur, CNRS, Laboratoire Lagrange, Bd de l'Observatoire, CS 34229, 06304 Nice cedex 4, France*
[12]*European Space Agency, European Space Research and Technology Centre (ESA/ESTEC), Keplerlaan 1, 2201 AZ Noordwijk, The Netherlands*
[13]*School of Physics & Astronomy, University of Birmingham, Edgbaston, Birmingham B15 2TT, United Kingdom*
[14]*Institut Paul Émile Victor, Concordia Station, Antarctica*
[15]*Australian Centre for Astrobiology, UNSW Sydney, NSW 2052, Australia*
[16]*Space Telescope Science Institute, 3700 San Martin Drive, Baltimore, MD 21218, USA*
[17]*INCT, Universidad de Atacama, calle Copayapu 485, Copiapó, Atacama, Chile*
[18]*Departamento de Astronomía, Universidad de Chile, Camino El Observatorio 1515, Las Condes, Santiago, Chile*
[19]*Instituto de Física y Astronomía, Universidad de Vaparaíso, Casilla 5030, Valparaíso, Chile*
[20]*Dunlap Institute for Astronomy and Astrophysics, University of Toronto, 50 St. George Street, Toronto, Ontario M5S 3H4, Canada*
[21]*Cerro Tololo Inter-American Observatory, Casilla 603, La Serena, Chile*
[22]*Department of Physics and Astronomy, The University of North Carolina at Chapel Hill, Chapel Hill, NC 27599-3255, USA*
[23]*Department of Physics and Kavli Institute for Astrophysics and Space Research, Massachusetts Institute of Technology, Cambridge, MA 02139, USA*
[24]*Department of Earth, Atmospheric, and Planetary Sciences, Massachusetts Institute of Technology, Cambridge, MA 02139, USA*
[25]*NASA Ames Research Center, Moffett Field, CA 94035, USA*
[26]*Department of Physics and Astronomy, University of New Mexico, Albuquerque, NM, USA*
[27]*Space Telescope Science Institute, 3700 San Martin Drive, Baltimore MD 21218*
[28]*NASA Goddard Space Flight Center, 8800 Greenbelt Road, Greenbelt, MD 20771, USA*
[29]*SETI Institute, Mountain View, CA 94043, USA*

(Received July 25, 2020; Revised —; Accepted —)

Submitted to AAS journals.

ABSTRACT

We report the discovery of TOI 837.01 and its validation as a transiting planet. We characterize the system using data from the NASA TESS mission, the ESA Gaia mission, ground-based photometry from El Sauce and ASTEP400, and spectroscopy from CHIRON, FEROS, and Veloce. We find that TOI 837 is a $T = 9.9$ mag G0/F9 dwarf in the southern open cluster IC 2602. The star and planet are therefore 35^{+11}_{-5} million years old. Combining the transit photometry with a prior on the stellar parameters derived from the cluster color-magnitude diagram,

Corresponding author: L. G. Bouma
luke@astro.princeton.edu

we find that the planet has an orbital period of 8.3 d and is slightly smaller than Jupiter ($R_{\rm p} = 0.80^{+0.09}_{-0.03}\,R_{\rm Jup}$). The transits are either grazing or nearly grazing. From radial velocity monitoring, we limit $M_{\rm p}\sin i$ to less than 1.20 $M_{\rm Jup}$ (3-σ). Grazing transits are a cause for concern, as they are often indicative of astrophysical false positive scenarios. Our follow-up data show that such scenarios are highly unlikely. Our combined multi-color photometry, high-resolution imaging, and radial velocities rule out hierarchical eclipsing binary scenarios. Background eclipsing binary scenarios, though limited by speckle imaging, formally remain a 0.2% possibility. TOI 837.01 is therefore a validated adolescent exoplanet. The planetary nature of the system can be confirmed or refuted through observations of the stellar obliquity or the planetary mass. Such observations may also improve our understanding of how the physical and orbital properties of exoplanets change in time.

Keywords: Exoplanets (498), Transits (1711), Exoplanet evolution (491), Stellar ages (1581), Young star clusters (1833)

1. INTRODUCTION

Over the first 100 million years of their lives, exoplanet systems are expected to undergo major physical and dynamical changes. For a typical Sun-like star, the protoplanetary disk disperses within roughly 1–10 million years (Mamajek 2009; Fedele et al. 2010; Dullemond & Monnier 2010; Williams & Cieza 2011). Gas giants presumably finish accreting before the end of disk dispersal (Pollack et al. 1996). While rocky planets may fully form within only a few million years (Dauphas & Pourmand 2011), they can also undergo significant growth over the next 10–100 million years through giant impacts (*e.g.*, Kleine et al. 2009; König et al. 2011; Morbidelli et al. 2012; Raymond et al. 2014). The Moon, for instance, may have formed from debris ejected during a collision between the proto-Earth and a planetesimal during Earth's first 100 million years (Cameron & Ward 1976; Canup & Asphaug 2001).

A number of other processes are expected to shape young exoplanets. After accreting, planets with gaseous envelopes are thought to cool and contract, and their atmospheres are expected to undergo photoevaporation (*e.g.*, Fortney et al. 2007; Owen & Wu 2013; Fulton et al. 2017; Gupta & Schlichting 2019, 2020). The relative importance of contraction and photoevaporation is set by the planetary mass, as well as the radiation environment. The effectiveness of photoevaporation can be inferred from observations of planetary winds in the metastable 1083 nm He line (Spake et al. 2018; Oklopčić & Hirata 2018; Mansfield et al. 2018).

Beyond physical changes, dynamical changes are expected in the semi-major axes, eccentricities, and stellar obliquities of young planets. When the gas disk is present, the planetary semi-major axis is thought to change in step with the viscous evolution of the disk (Lin et al. 1996). High-eccentricity migration processes including planet-planet scattering, secular chaos, and Kozai-Lidov oscillations can also occur (*e.g.*, Chatterjee et al. 2008; Lithwick & Wu 2014; Fabrycky & Tremaine 2007). The circularization timescale is thought to be such that for any giant planets that migrated early, their orbits should circularize within 100 million years (Zahn 1977).

Finding and studying systems undergoing these evolutionary changes is a major goal in contemporary exoplanet research. To identify stars younger than say 1 Gyr, a number of direct and indirect methods are available (Soderblom 2010). The traditional approach is to isochronally age-date coeval groups of stars, hereafter "clusters" (*e.g.*, Lada & Lada 2003; Zuckerman & Song 2004; Krumholz et al. 2019). Young field stars can also be identified isochronally, provided that they are sufficiently massive (Berger et al. 2020). Other age indicators include stellar rotation periods, the abundance of photospheric lithium, and chromospheric diagnostics such as calcium emission and broadband UV emission. Studies by, for instance, David et al. (2018) and G. Zhou et al. (2020, submitted) have combined these methods to age-date individual field stars hosting transiting planets. Many of these latter methods were summarized by Mamajek & Hillenbrand (2008), and have since been calibrated by, *e.g.*, Irwin & Bouvier (2009); Barnes et al. (2015); Meibom et al. (2015); Angus et al. (2015) and Curtis et al. (2019b) for stellar rotation, Žerjal et al. (2017) for chromospheric activity, and *e.g.*, Berger et al. (2018) and Žerjal et al. (2019) for lithium abundances.

A few dozen planets in clusters have been detected, and fewer still have been closely characterized. Despite the challenges of starspot-induced radial velocity (RV) variations, RV surveys found success in the Hyades, NGC 2523, Praesepe, and M 67 (Sato et al. 2007; Lovis & Mayor 2007; Quinn et al. 2012; Malavolta et al. 2016; Brucalassi et al. 2017). RV surveys of highly active pre-main sequence stars in Taurus also led to the youngest hot Jupiters yet reported (Donati et al. 2016; Johns-Krull et al. 2016; Yu et al. 2017; Biddle et al. 2018; Flagg et al. 2019).

The transit method was comparatively slow to catch up. Early deep transit searches of open clusters by many groups did not yield definitive planet detections (Mochejska et al. 2005, 2006; Burke et al. 2006; Aigrain et al. 2007; Irwin et al. 2007; Miller et al. 2008; Pepper et al. 2008; Hartman et al. 2009). These searches were typically sensitive to planets larger than Jupiter, on $\lesssim 3$ day orbital periods. Hot Jupiter occurrence rate limits were derived at the $\lesssim 5\%$ level (*e.g.*, Burke et al. 2006; Hartman et al. 2009). The modern 0.5-1% occurrence rate suggests that these early transit surveys would have needed a greater data volume at higher precision for detection to be possible (Mayor et al. 2011; Wright et al. 2012; Howard et al. 2012; Petigura et al. 2018).

Kepler observed a large enough number of stars with sufficient baseline and precision to detect transiting planets in open clusters: Kepler-66b and 67b, in the gigayear-old NGC 6811 (Borucki et al. 2010; Meibom et al. 2013). Though a broken reaction wheel ended the prime Kepler mission, the repurposed K2 (Howell et al. 2014) switched between fields along the ecliptic every quarter-year, and was able to observe far more clusters and young stars.

The discoveries made by K2 through its surveys of Taurus, the Hyades, Praesepe, and Upper Sco were a major inspiration for the present work (*e.g.*, Mann et al. 2016a; Obermeier et al. 2016; Mann et al. 2017; Vanderburg et al. 2018; Ciardi et al. 2018; Livingston et al. 2018; Mann et al. 2018; Rizzuto et al. 2018; Livingston et al. 2019). Observations with K2 convincingly showed that at least some close-in planets must form within about 10 Myr (Mann et al. 2016b; David et al. 2016). They also led to the first hints that young planets in clusters may in fact be qualitatively different from their field counterparts. For instance, based on its observed mass, radius, and UV environment, the 700 Myr K2-100b is probably actively losing its atmosphere, and should become a bare rocky planet over the next few hundred Myr (Mann et al. 2017; Barragán et al. 2019). The four transiting planets around V1298 Tau (23 Myr) are also likely to be photoevaporating, and could represent a precursor to Kepler's compact multiple systems (David et al. 2019a,b).

With the aim of advancing the young planet census, we have been using data from the TESS spacecraft (Ricker et al. 2015) to perform a Cluster Difference Imaging Photometric Survey (CDIPS; Bouma et al. 2019). Our targets in this survey are candidate young stars that have been reported in the literature. At the time of writing, we had made $\sim 6 \times 10^5$ light curves from the first year of TESS observations. The light curves are available at MAST[1]. Searching through a subset of these light curves brought our attention to the candidate transiting planet, TOI 837.01, that is the subject of this analysis.

The transits of TOI 837.01 are grazing, which is a cause for concern. Particularly for a target near the galactic plane ($b = -5.8°$), background eclipsing binaries are a major source of astrophysical false positives (*e.g.*, Sullivan et al. 2015, Figure 30). Our follow-up data show that this and related scenarios are unlikely to the degree that we can "validate" the planet, *i.e.*, determine that its probability of being an astrophysical false positive is negligibly small. We considered this result worth reporting because of the planet's youth.

Section 2 describes the identification of the candidate, and our follow-up observations. Section 3 combines the available data to assess the system's false positive probability, and validates TOI 837.01 as a planet. Section 4 presents our knowledge of the cluster (Section 4.1), the star (Section 4.2) and the planet (Section 4.3). We conclude by discussing avenues for confirmation and improved characterization in Section 5.

[1] ARCHIVE.STSCI.EDU/HLSP/CDIPS, and see DOI.ORG/10.17909/T9-AYD0-K727

2. IDENTIFICATION AND FOLLOW-UP OBSERVATIONS

2.1. *TESS Photometry*

TOI 837 was observed by TESS from 26 March 2019 until 20 May 2019, during the tenth and eleventh sectors of science operations (Ricker et al. 2015). The star was designated TIC 460205581 in the TESS Input Catalog (Stassun et al. 2018, 2019). Pixel data for an 11×11 array surrounding the star were averaged and saved at 2-minute cadence. The 2048×2048 image from the entire CCD was also averaged into 30-minute stacks, and saved as a "full frame image" (FFI).

The TESS project detected the transits in the 2-minute data and the community was alerted on 17 June 2019. Our subsequent blind search of the CDIPS FFI light curves also showed the transits. Given that the 2-minute data had better sampling cadence, we opted to use the Presearch Data Conditioning (PDC) light curve with the default aperture for our analysis (Smith et al. 2012; Stumpe et al. 2014; Jenkins et al. 2016; Smith et al. 2016).

Figure 1 shows the data. The dominant modulation induced by starspots coming into and out of view has a peak-to-peak amplitude of about 2.3%, and a period of about 3 days. The dips suggestive of a grazing transiting planet recur roughly every 8 days, and have a depth of about 0.4%. A few flares are also visible. A phase-folded view of the TESS transits with starspot variability removed is shown in Figure 1. Our fitting procedure for the models shown in these plots is described in Section 4.3.

2.2. *Gaia Astrometry and Imaging*

Between 25 July 2014 and 23 May 2016, the ESA Gaia satellite measured about 300 billion centroid positions of 1.6 billion stars. The positions, proper motions, and parallaxes of the brightest 1.3 billion were calculated for the second data release (DR2) (Gaia Collaboration et al. 2016; Lindegren et al. 2018; Gaia Collaboration et al. 2018). TOI 837 was assigned the Gaia DR2 identifier 5251470948229949568, and had 276 "good" astrometric observations. Its brightness was measured in the G, Rp, and Bp bands of the Radial Velocity Spectrometer (Cropper et al. 2018; Evans et al. 2018).

The Gaia imaging, reduced to its point-source catalog, provides the initial context for analyzing the TESS data. Stars brighter than $T = 16$, as queried from the Gaia DR2 source catalog, are shown with white circles in Figure 2, overlaid on the TESS image. Given its galactic latitude of $b = -6°$, it is not surprising that the field of TOI 837 is crowded. The resolved stars that were of immediate concern for our false positive analysis were as follows.

- TOI 837 $\equiv$ TIC 460205581 ($T = 9.9$). The target star.

- Star A $\equiv$ TIC 847769574 ($T = 14.6$), 2.3″ West. The proper motions and parallax of this star imply it is comoving with TOI 837 and that the two stars are separated by 6.6 ± 0.1 pc. Star A is therefore likely an

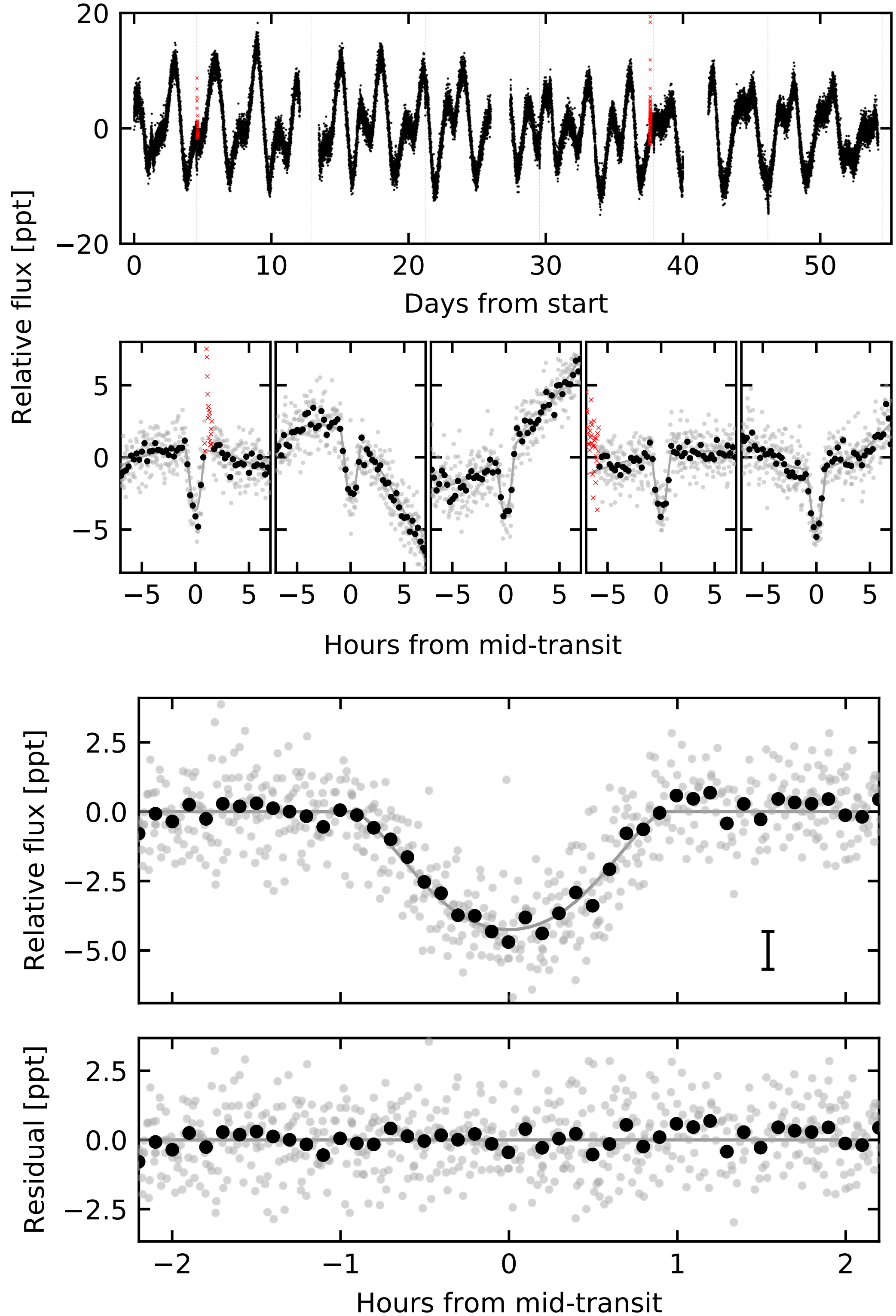

Figure 1. TESS light curve of TOI 837. *Top*: PDCSAP median-subtracted relative flux at 2-minute sampling in units of parts-per-thousand ($\times 10^{-3}$). Starspot-induced variability is the dominant signal; flares are shown with red crosses. Dashed lines indicate the five transits observed by TESS over Sectors 10 and 11. *Middle*: Individual transits. Gray lines are the best-fit transit model, which includes a local quadratic trend in each window. Gray points are 2-minute PDCSAP flux measurements, black points are binned to 15-minute intervals. *Bottom*: Phase-folded TESS transit. Gray points are 2-minute measurements with the local spot-induced variation removed. Binning at 6-minute intervals yields the black points. The black error-bar shows the median uncertainty for the black points. The gray line shows the best-fit model to the TESS data.

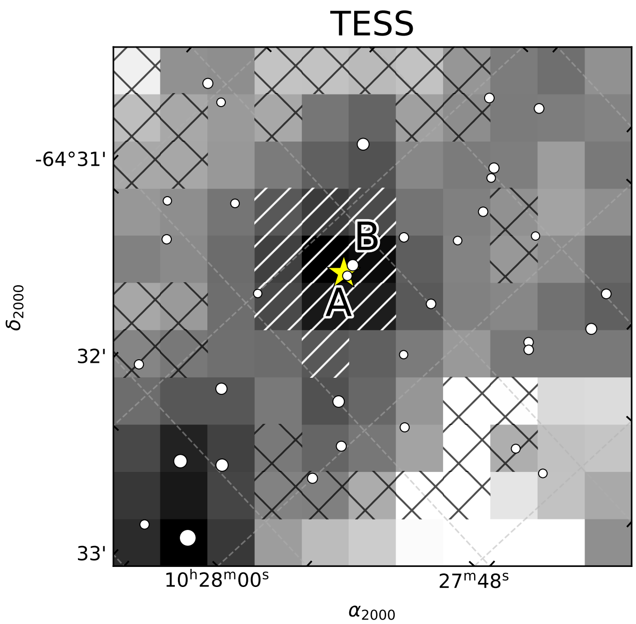

Figure 2. Scene of TOI 837. Mean TESS image of TOI 837 over Sector 10, with a logarithmic grayscale. The yellow star is the position of TOI 837. White circles are resolved Gaia sources with $T < 16$ (brighter stars are larger). The black X and white / hatches show the apertures used to measure the background and target star flux, respectively. Dashed lines of constant declination and right ascension are shown. Two stars of interest are "Star A" and "Star B", which were eventually excluded as being possible sources of the transits.

IC 2602 member, but unlikely to be a bound binary companion.

- Star B ≡ TIC 460205587 (T = 13.1), 5.4″ North. The Gaia parallax implies this is a giant background star.

An additional source, TIC 847769581, is 4.9″ from the target, but too faint (T = 18.8) to be the source of the observed transit signal.

The Gaia DR2 data for Star A seems poorly behaved. While Star A has G = 15.1, and Bp = 14.9, no Rp magnitude is reported. Correspondingly, no RUWE[2] value is available. We suspect that the photometric failure to produce an Rp magnitude as well as its poor astrometric fit are due to blending with TOI 837.

At the ≈ 1′ resolution of the TESS data, if either Star A or Star B were eclipsing binaries, they could be the sources of the transit signal. A detailed analysis of ground-based seeing-limited photometry was necessary to assess and rule out this possibility (Section 2.4).

2.3. *High-Resolution Imaging*

To determine if any fainter point sources existed closer to TOI 837 inside of Gaia's point-source detection limits, we acquired high-resolution speckle images. We then searched the autocorrelation functions of these images for peaks indicative of nearby companions.

The observations of TOI 837 were initially acquired by Ziegler et al. (2020) as part of the Southern Astrophysical Research (SOAR) TESS Survey using the High Resolution Camera (HRCam; Tokovinin 2018). The HRCam I-band filter is described by Tokovinin (2018). The points in Figure 4 show the resulting measured 5-σ detectable contrasts. The lines are linear smoothing fits between the regimes of the diffraction limit, the "knee" at ≈ 0.2″, and the slow decrease until ≈ 1.5″, beyond which the speckle patterns become de-correlated. Star A (TIC 847769574) was detected at the expected location and brightness contrast, and no additional companions were found. Star B was not detected; with a separation of 5.4″ from TOI 837, it fell outside the field of view.

2.4. *Ground-based Time-Series Photometric Follow-up*

We obtained ground-based seeing-limited time series photometric observations of TOI 837 bracketed around the times of transit. These observations confirmed that the transits occurred on-target to within ≈ 2″, and that they were achromatic. Both features are essential for our ability to eliminate false-positive scenarios.

2.4.1. *El Sauce 0.36 m*

Acquisition and reduction—We observed four transits with the 0.36 m at Observatorio El Sauce, located in the Río Hurtado Valley in Chile, and operated by co-author P. Evans. The observations were obtained in Cousins-R band on the nights of 1 April 2020 and 26 April 2020, Cousins-I band on the night of 21 May 2020, and Johnson-B band on the night of 14 June 2020. The final 14 June transit began shortly after twilight.

We scheduled our transit observations using the `TESS Transit Finder`, which is a customized version of the `Tapir` software package (Jensen 2013). The photometric data were calibrated and extracted using `AstroImageJ` (Collins et al. 2017). Comparison stars of similar brightness were used to produce the final light curves, each of which showed a roughly 4 ppt dip near the expected transit time. The data are reported in Table 1 and plotted in Figure 3.

Custom aperture analysis—Based solely on the TESS data, both Star A and Star B were possible sources of blended eclipsing binary signals. The typical FWHM for stars in the El Sauce observations was ≈ 2.3″, with a variance of ≈ 0.2″. Star B is resolved in the 0.36 m images; Star A is not.

To rule out blend scenarios with the ground-based photometry, we produced light curves centered on TOI 837 with circular apertures of radii ranging from 0.7″ to 5.1″. We did not detect any statistically significant variation in the depth of the transits with aperture size. Two lines of evidence rule out Star B as the eclipsing source: first, the transits were detected in

[2] See the Gaia DPAC technical note GAIA-C3-TN-LU-LL-124-01, http://www.rssd.esa.int/doc_fetch.php?id=3757412, `2020-07-08`.

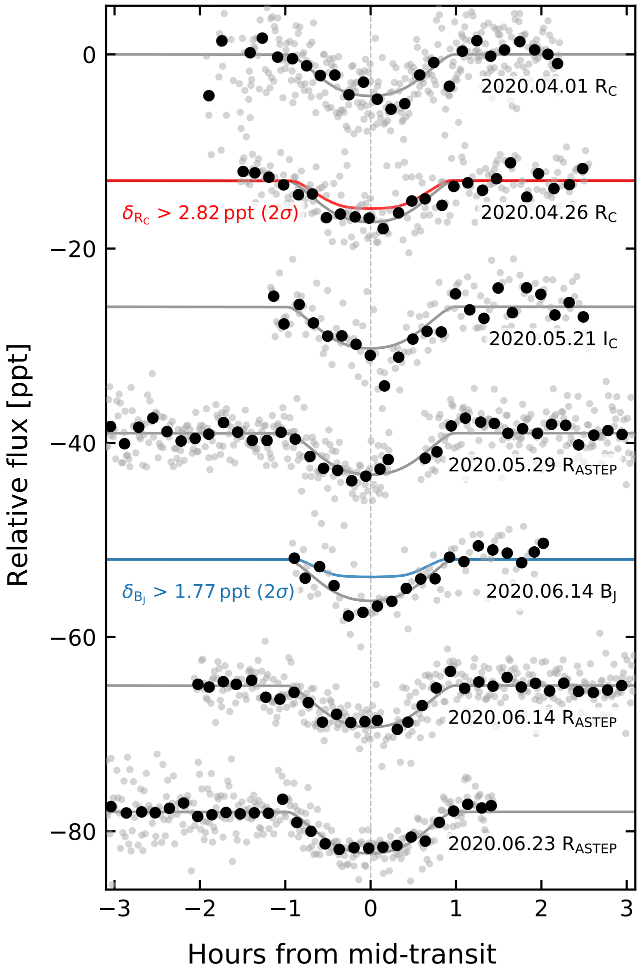

Figure 3. Ground-based follow-up photometry. The data were acquired using the 0.36 m at El Sauce and the 0.40 m ASTEP400 at Dome C. Black points are binned to 10-minute intervals. The gray line is the best-fit model to the combined TESS and ground-based data. Red and blue lines show 2-σ lower limits on the transit depths in the Cousins-R and Johnson-B bandpasses used to rule out specific false positive scenarios (see Section 3.1.5).

the smallest apertures. Second, we made light curves with 2.1″ apertures centered on Star B, and they did not show the transit.

To assess the possibility that Star A is an eclipsing body, we created light curves with a custom set of circular apertures with radii of 2.1″ and positions ranging from Star A (2.3″ West of TOI 837) to 2.3″ East of TOI 837. We did not detect any variation of the transit depth along this line of light curves. The apertures East of TOI 837 exclude over 90% of the flux from Star A. The eclipse on Star A would therefore need to have depth greater than unity to produce the observed eclipse depth. We therefore interpret the lack of asymmetry between the Western-most (centered on Star A) and Eastern-most (furthest from Star A) light curves as conclusive evidence that TOI 837 is the source of the transit signal to within ≈ 2.0″. To verify self-consistency, we checked that the maximum dilution from Star A (≈ 1%) is less than the uncertainty of the transit depth measurements (≈ 15%), and so the lack of variation of transit depth with aperture location is consistent with TOI 837 being the source of transits.

2.4.2. *ASTEP400*

We observed three transits with the 0.40 m ASTEP telescope at the Concordia base on the Antarctic Plateau (Daban et al. 2010). Concordia base is operated jointly by the French and Italian polar institutes, IPEV and PNRA. Its position on the Antarctic Plateau allows it to take advantage of the continuous night during Austral winter. The weather is of photometric quality for about two-thirds of each winter (Crouzet et al. 2018).

ASTEP is equipped with a FLI Proline science camera with a KAF-16801E, 4096 × 4096 front-illuminated CCD. The camera has an image scale of 0.93 arcsec pixel^{-1} resulting in a 1° × 1° corrected field of view. The focal instrument dichroic plate splits the beam into a blue wavelength channel for guiding, and a non-filtered red science channel roughly matching a Cousins-R transmission curve (Abe et al. 2013; Mékarnia et al. 2016). The images were processed on-site using an automated aperture photometry pipeline based on the `daophot` package of the IDL astronomy user's library (Landsman 1995).

TOI 837 was observed with ASTEP on 12 May 2020, 29 May 2020, 14 June 2020, and 23 June 2020 (UT) with a cadence of 50 s (exposure time of 25 s, readout and processed overhead of 25 s). Except for 12 May, our observations were conducted under stable weather conditions, with clear skies, temperatures of about −70°C, and wind speeds less than 5 m s^{-1}. Due to their poor quality, we exclude from the analysis all data collected on May 12. We found that the optimal calibrated light curves of TOI 837 correspond to an 11 pixel (10 arcsec) and 14 pixel (12 arcsec) radius aperture for observations carried out on June and May, respectively. The data are reported in Table 1, and plotted in Figure 3.

Table 1. Ground-based TOI 837 photometry.

Time [$BTJD_{TDB}$]	Rel. Flux	Rel. Flux Err.	Instrument
1940.487018	0.999998	0.002430	El Sauce
1998.700107	0.998675	0.001621	ASTEP

NOTE— Table 1 is published in its entirety in a machine-readable format. Two example entries are shown for guidance regarding form and content. To convert from BTJD to BJD, add 2,457,000.

2.5. *Spectroscopic Follow-up*

Reconnaissance spectroscopic follow-up is an essential step in vetting planet candidates. Medium to high-resolution spectra enable physical characterization of the star and therefore planet. Reducing multiple spectra to a radial velocity time-series can enable planet mass measurements, and also set limits on the mass of any nearby companions. Finally, if there are close or bright companions, reconnaissance spectra can also reveal the presence of a secondary set of stellar lines.

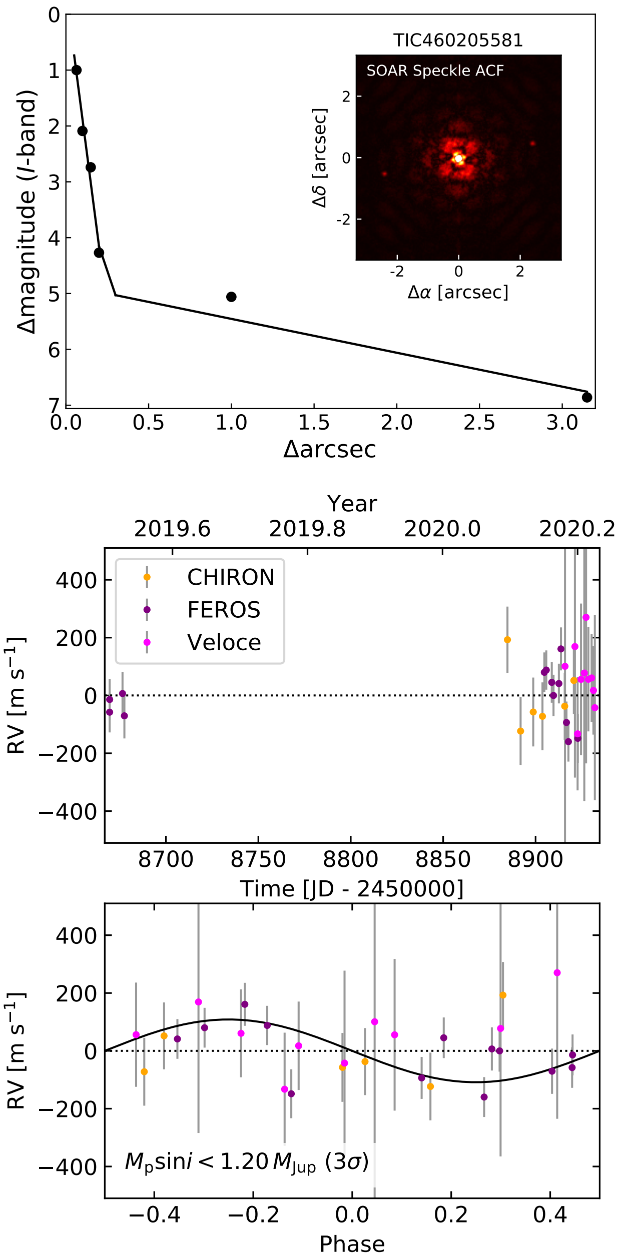

Figure 4. Speckle-imaging and velocimetry of TOI 837. *Top:* SOAR HRCam contrast limits derived from point-source injection-recovery experiments. Star A ($\Delta T = 4.7$, $2.3''$ West) is detected, and is also a resolved Gaia source. It is co-moving with TOI 837, and its parallax and on-sky position imply that it is physically separated from TOI 837 by 6.6 ± 0.1 pc. *Middle:* Radial velocity (RV) measurements, with best-fit instrument offsets and jitter terms included. The expected scatter from starspots based on $v\sin i$ and the photometric modulation amplitude is of order 300m s^{-1}. *Bottom:* RV measurements phased to the orbital ephemeris of TOI 837.01. The planet is not detected. The black line shows a circular Keplerian orbit representing the 3-σ upper mass limit.

2.5.1. *SMARTS 1.5 m / CHIRON*

We acquired nine spectra using CHIRON at the SMARTS 1.5 m telescope at Cerro Tollo Inter-American Observatory, Chile (Tokovinin et al. 2013). Six met our signal-to-noise requirements for radial velocity measurements and stellar parameter extraction. We used CHIRON in its image slicer configuration, yielding a spectral resolution of ≈ 79,000 across 415–880 nm.

We derived radial velocities and spectroscopic line profiles from the CHIRON observations using a least-squares deconvolution of the spectra against non-rotating synthetic spectral templates (Donati et al. 1997). The spectral templates were generated using ATLAS9 atmosphere models (Castelli & Kurucz 2004) with the `SPECTRUM` script (Gray & Corbally 1994). These line profiles were fitted with a broadening kernel that describes the rotational, radial-tangential macroturbulent, and instrumental broadening of the spectrum. The rotational and macroturbulent broadening are computed per Gray (2005), following the methods described in Zhou et al. (2018). We fitted the line profile from each observation independently, yielding the radial velocities listed in Table 2 and shown in Figure 4. We found a mean rotational broadening velocity of $v\sin I_\star = 16.2 \pm 1.1\,\mathrm{km\,s^{-1}}$, and a macroturbulent broadening of $v_{\rm Mac} = 8.4 \pm 2.9\,\mathrm{km\,s^{-1}}$.

To derive the stellar parameters, we matched the set of CHIRON spectra against a library of observed spectra, previously obtained using the Tillinghast Reflect Echelle Spectrograph (TRES, Fűrész et al. 2008) on the 1.5 m reflector at the Fred Lawrence Whipple Observatory (FLWO), Arizona, USA, and classified using the Stellar Parameter Classification pipeline (Buchhave et al. 2010). We found the best matching stellar parameters to be $T_{\rm eff} = 5899 \pm 55$K, $\log g = 4.496 \pm 0.011$ dex, and $[{\rm Fe/H}] = -0.069 \pm 0.042$ dex. We ultimately adopted a different set of stellar parameters for our analysis (see Section 4.2.4).

The spectroscopic line profiles were thoroughly examined for any signs of secondary lines that might indicate the presence of another star, either associated or in chance alignment with TOI 837. No such set of lines were found. To determine our detection limits to a blended spectroscopic companion, we injected a second set of lines to the mean least-squares deconvolution profile derived from the CHIRON observations. The injection spanned 10,000 different combinations of line broadening, velocity separation, and flux ratio F_2/F_1. The recovery results showed that for rotational broadenings of the secondary of 5, 15, and 25 km s^{-1}, we were able to exclude sources with flux fractions F_2/F_1 brighter than roughly 0.03, 0.08, and 0.20, provided that the secondary was separated from the primary by at least ≈ 15 km s^{-1}. At smaller velocity separations, the injected lines begin to blend with the target spectrum.

2.5.2. *FEROS*

TOI 837.01 was monitored with the FEROS echelle spectrograph (Kaufer et al. 1999), mounted on the MPG 2.2 m telescope at the ESO La Sille Observatory, in Chile. FEROS has a resolution of ≈48,000 across a spectral range of 350–920 nm. It has a remarkably high efficiency of ≈20%. We obtained 13 spectra of TOI 837 between July 5 of 2019 and March 14 of 2020 in the context of the Warm gIaNts with tEss (WINE) collaboration, which focuses on the systematic characterization of TESS transiting giant planets with moderately long orbital periods (*e.g.*, Brahm et al. 2019; Jordán et al. 2020). We adopted exposure times of 500 and 600 seconds and the observations were performed with the simultaneous calibration mode for tracing the instrumental velocity variations with a comparison fiber illuminated with a ThAr lamp. FEROS data was processed with the `ceres` pipeline (Brahm et al. 2017), which delivers precision radial velocities and bisector span measurements through cross-correlation of the extracted spectra with a binary mask resembling the properties of a G2V star. The radial velocities are given in Table 2, and shown in Figure 4. To check for the presence of secondary lines, we performed a similar injection-recovery exercise as with the CHIRON data. We achieved slightly worse limits, likely due to the lower spectral resolution of FEROS, and therefore adopted the CHIRON limits.

2.5.3. *Veloce*

We acquired 34 spectra over 10 visits of TOI 837 using the Veloce spectrograph, mounted on the AAT 3.9 m telescope at Siding Spring Observatory near Coonabarabran, Australia (Gilbert et al. 2018). In the "Rosso" instrument-mode, Veloce provides coverage from 600–950 nm at a spectral resolution of ≈ 80,000. Many of the exposures were taken in average or poor seeing conditions, when fiber-to-fiber cross-contamination on the IFU-style fiber feed is strongest. To reduce the spectra to velocities, we cross-correlated against a high S/N template of δ Pavonis, because with spectral type G8 IV it was the closest TOI 837 analog available in the Veloce spectral database. The velocity RMS seen across each visit was hundreds of meters per second, likely due to uncorrected fiber-to-fiber cross-contamination. For analysis purposes, we averaged across each visit, and set the velocity uncertainties to be the standard deviation of the per-visit exposures. The velocities are given in Table 2, and shown in Figure 4.

Table 2. TOI 837 radial velocities.

Time [$\mathrm{BJD_{TDB}}$]	RV [$\mathrm{m\,s^{-1}}$]	σ_{RV} [$\mathrm{m\,s^{-1}}$]	Instrument
8669.533150	-57.80	27.50	FEROS
8669.540450	-13.90	29.40	FEROS
8676.506930	6.70	37.80	FEROS
8677.519150	-70.30	44.60	FEROS
8884.787630	240.00	28.00	CHIRON
8891.891180	-76.00	37.00	CHIRON
8898.735330	-10.00	43.00	CHIRON
8903.725760	-25.00	38.00	CHIRON
8904.739930	80.10	24.50	FEROS
8905.793630	88.00	21.70	FEROS

Table 2 *continued*

Table 2 *(continued)*

Time [$\mathrm{BJD_{TDB}}$]	RV [$\mathrm{m\,s^{-1}}$]	σ_{RV} [$\mathrm{m\,s^{-1}}$]	Instrument
8908.762520	45.30	28.30	FEROS
8909.702140	0.00	31.80	FEROS
8912.606750	41.30	24.10	FEROS
8913.740580	161.10	37.30	FEROS
8915.762170	10.00	33.00	CHIRON
8916.714540	-93.50	33.60	FEROS
8917.765720	-159.70	24.80	FEROS
8920.706100	99.00	32.00	CHIRON
8922.845800	-148.30	54.90	FEROS
8915.924027	37.51	725.91	Veloce
8921.284950	105.90	453.19	Veloce
8922.733572	-195.92	195.63	Veloce
8924.583708	-7.65	262.32	Veloce
8926.365810	14.28	442.64	Veloce
8927.318146	207.04	505.19	Veloce
8928.559780	-7.28	180.24	Veloce
8930.324059	-2.60	152.02	Veloce
8931.293091	-45.68	152.94	Veloce
8932.065206	-105.60	319.82	Veloce

3. ELIMINATION OF FALSE POSITIVE SCENARIOS

Validating a transiting planet means statistically arguing that the data are much more likely to be explained by a planet than by an astrophysical false positive. The concept of validation has been developed and calibrated by *e.g.*, Torres et al. (2011); Morton (2012); Díaz et al. (2014); Santerne et al. (2015); Morton et al. (2016) and Giacalone & Dressing (2020). "Validation" is different from "confirmation", which means that there is overwhelming evidence that the transits *must* be explained by a planet, through elimination of all false positive scenarios and determination that the planety's mass is in the substellar regime.

Assuming an eclipse has been localized to the target star, potential false positive scenarios include eclipses of a background binary (BEB), eclipses of a hierarchical system bound to the primary star (HEB), and the possibility that the eclipses are simply caused by a stellar companion, rather than a planetary one (EB).

Figure 5 provides a visual summary of the possible astrophysical false positive scenarios, as well as our ability to rule them out based on our combined photometry, velocimetry, and imaging. In this Section we describe each constraint in turn, and then present a calculation using `VESPA` (Morton 2012) to demonstrate that the probability TOI 837 is an astrophysical false positive is small enough to formally validate it as a planet.

3.1. *Constraints on False Positive Scenarios*

3.1.1. *Transit Depth*

In HEB and BEB scenarios, the flux from TOI 837 and the true eclipsing binary host blend together, and reduce the "true" eclipse depth δ_{true} to the observed depth δ_{obs}:

$$\delta_{\mathrm{obs}} = \delta_{\mathrm{true}} \frac{F_{\mathrm{comp}}}{F_{\mathrm{total}}}, \tag{1}$$

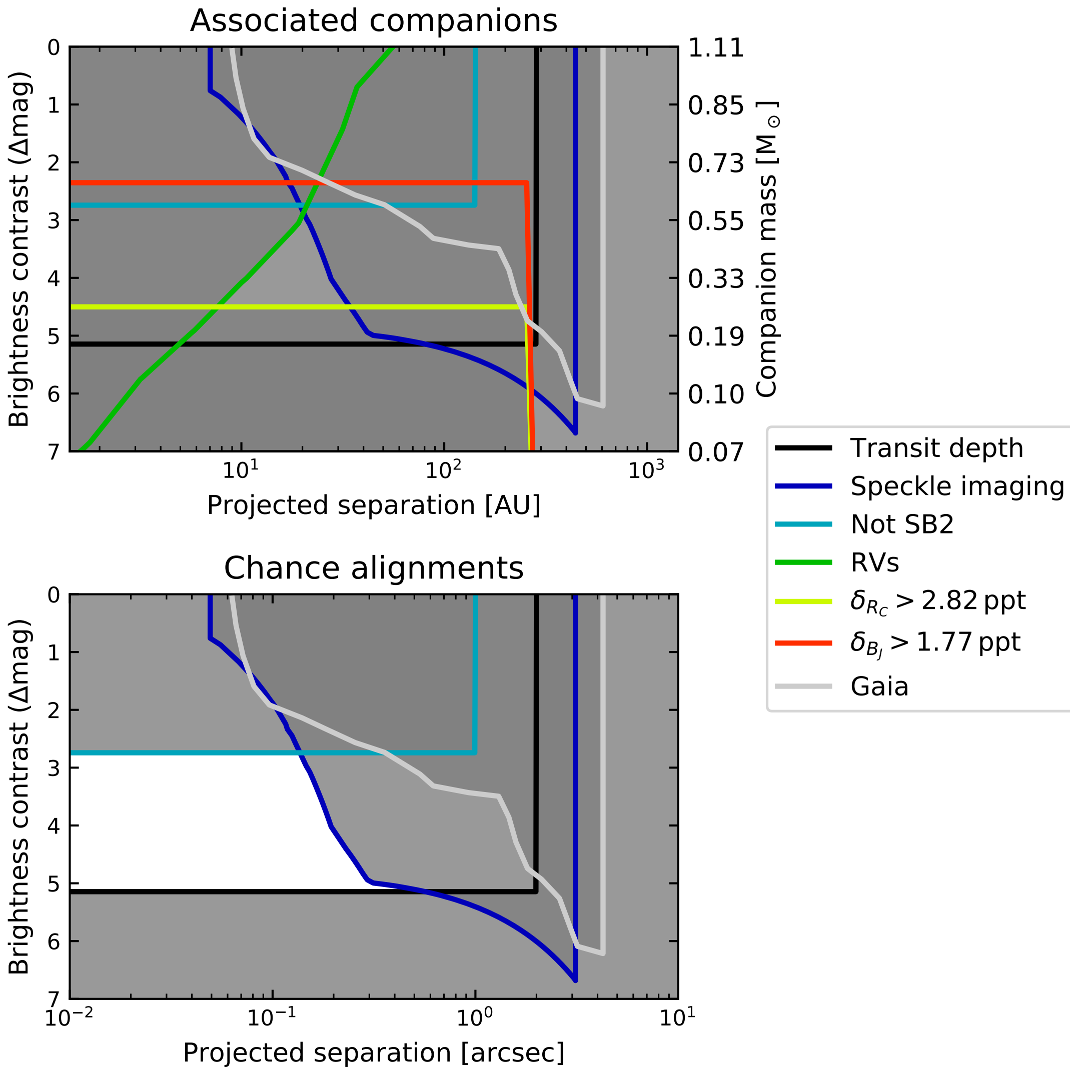

Figure 5. Astrophysical false positive scenarios. *Top*: for bound companions (EB and HEB scenarios), *Bottom*: for unassociated companions along the same line of sight (BEB scenarios). Each constraint is described in Section 3.1. Gray regions are ruled out by at least one constraint.

where the total system flux and the flux from only the companion ("comp") binary are labeled appropriately. The requirement that the eclipse is produced by fusion-powered stars and that $\delta_{\rm true} < 0.5$ translates to a bound on the faintest possible blended companion system:

$$\Delta m < -\frac{5}{2}\log_{10}\left(\frac{0.5}{\delta_{\rm obs}}\right). \tag{2}$$

For TOI 837 ($T = 9.93$), this implies that any stellar companion invoked to explain the transit depth must be brighter than $T = 15.07$. In Figure 5, we set the spatial limit to $2''$ based on the precision at which we have localized the transits using seeing-limited ground-based photometry.

If the transit were box-shaped, this argument could be extended to even more restrictive depths (*e.g.*, Seager & Mallén-Ornelas 2003; Vanderburg et al. 2019; Rizzuto et al. 2020). Since the transits of TOI 837 could be grazing, the second and third contact points do not necessarily occur, and the shape of the transit is not particularly restrictive.

3.1.2. *Speckle Imaging*

The contrast limits obtained through the SOAR *I*-band speckle imaging (Section 2.3) are shown in Figure 5. While "Star A" was detected in the SOAR images, our ground-based photometry rules it out as a possible source of the eclipse signal (Section 2.4). To convert the remaining contrast constraints to limits on the masses of bound companions, we used the Baraffe et al. (2003) models for sub-stellar mass objects and the MIST models for stellar mass objects (Paxton et al. 2011, 2013, 2015; Dotter 2016; Choi et al. 2016). We assumed that the system age was 35 Myr, so that companions would be at a plausible state of contraction.

To convert from theoretical effective temperatures and bolometric luminosities to expected magnitudes in instrumental bandpasses, we made the simplifying assumption that all sources had blackbody spectra. Using the theoretical stellar parameters and the measured transmission functions (Tokovinin 2018), we then calculated the apparent magnitudes of stellar companions of different masses, and interpolated to produce the scale shown on the upper-right in Figure 5.

3.1.3. *Not SB2*

We determined our detection limits to blended spectroscopic companions using the stacked CHIRON spectra (see Section 2.5.1). For a slowly rotating stellar companion well-separated in velocity, this would have revealed companions with flux fractions $F_2/F_1 \gtrsim 3\%$. For a companion with rotational broadening of $15\,\mathrm{km\,s^{-1}}$, roughly equivalent to that of TOI 837, we were able to exclude companions with flux fractions exceeding ≈8%. For plotting purposes, in Figure 5 we have assumed the latter flux-fraction limit of 8% ($\Delta\mathrm{mag} \approx 2.7$). For bound companions this is justified through reasoning that coeval binary companions to TOI 837 would have both longer rotation periods and smaller stellar radii. The equatorial velocities of such companions would therefore be expected to be smaller than that of TOI 837.

3.1.4. *RVs*

The radial velocities from FEROS, CHIRON, and Veloce can be used to detect massive bound companions orbiting TOI 837. We searched for the presence of planetary and stellar-mass companions using `radvel` (Fulton et al. 2018). We assumed circular orbits, and performed two sets of fits.

For the first fit we set a prior on the period and time of periapse using the known ephemeris from the transit. We then fitted for the semi-amplitude, instrument offsets, and jitter parameters. This yielded a non-detection of the planet's orbit. The corresponding 3-σ (99.7$^{\mathrm{th}}$ percentile) upper limit on $M_{\mathrm{p}}\sin i$ is $1.20 M_{\mathrm{Jup}}$. The data and corresponding model are shown in Figure 4.

The above exercise ruled out the possibility that the observed eclipses are caused by a stellar-mass object orbiting TOI 837. The lack of a linear radial velocity trend, particularly in the FEROS data, further constrains the presence of a hierarchical binary system. Fitting a line to the FEROS velocities, we found that any third body in the system would need to induce a linear radial velocity trend with amplitude $|\dot{\gamma}| < 0.82\,\mathrm{m\,s^{-1}\,day^{-1}}$, at 3-$\sigma$ confidence. The baseline of the FEROS data is 253 days; the agreement between the mean Gaia DR2 velocity ($17.44 \pm 0.64\ \mathrm{km\,s^{-1}}$) and that from FEROS ($18.0 \pm 0.1\,\mathrm{km\,s^{-1}}$) in theory places an additional limit on linear trends, since the two observation epochs are separated by roughly five years.

To place limits on the properties of a possible bound hierarchical companion, we fitted the radial velocity data for a Keplerian orbit using wide priors on the semi-amplitude and period: $\log K\ [\mathrm{m\,s^{-1}}] \sim \mathcal{U}(1, 10^5)$, and $\log P\ [\mathrm{days}] \sim \mathcal{U}(0.1, 10^{15})$. We then fitted for the semi-amplitude, period, time of conjunction, instrument offsets, and jitter parameters. We converted the resulting posterior in period and semi-amplitude to minimum mass and semi-major axis assuming Kepler's third law. The resulting 3-σ limits are shown in Figure 5.

3.1.5. *Multicolor Photometry*

Multicolor photometry and HEB scenarios —The most plausible HEB scenarios for TOI 837 involve pairs of eclipsing M dwarfs (Figure 5). Eclipses of such stars are much redder than eclipses of the G-dwarf TOI 837. Limits on whether the transit depth decreases in bluer bandpasses can therefore rule out some HEB scenarios.

We fitted for the observed depths in different bandpasses using a similar machinery as described in Section 4.3. We fitted each ground-based transit individually for the planet-to-star size ratio, the impact parameter, and a local quadratic trend (the ephemeris was assumed from an initial fit of only the TESS data). The corresponding 2-σ lower limits on the transit depths in Cousins-R and Johnson-B band light curves were 2.82 and 1.77 ppt, respectively, and are shown in Figure 3. Particularly in our Johnson-B light curve, the transit depth is correlated with the mean and linear slope of the light curve: a smaller depth is allowed if the data are fitted with a larger linear slope and a larger mean. Our quoted limits marginalize over these correlations, and the depth measurement itself is nearly Gaussian.

To determine what classes of HEB are eliminated by these limits, we performed the following calculation. We assumed that each system was composed of the primary (TOI 837), plus a tertiary companion eclipsing a secondary companion every 8.3 days. For secondary masses ranging from 0.07 to $1.10\,M_\odot$, and mass ratios (M_3/M_2) from 0.1 to 1, we then calculated the observed maximal eclipse depth caused by Star 3 eclipsing Star 2 in each observed bandpass. As before, we interpolated between mass, effective temperature, and radius assuming the MIST isochrones for a 35 Myr old system, and also assumed that each source had a blackbody spectrum. We used the transmission functions from the SVO filter profile service[3]. For a typical HEB system (*e.g.*, $M_2 = M_3 = 0.2 M_\odot$), the bluest optical bandpasses produced eclipses roughly 10 times shallower than in TESS-band, because the M-dwarf blackbody function turns over at much redder wavelengths than the G-dwarf blackbody (Wien's law).

For a fixed secondary mass, we then asked whether any tertiary companions existed for which the maximal expected eclipse depth could have been larger than the observed depth. In cases for which the answer was yes, we could not rule out such hierarchical eclipsing binary systems. Conversely, we ruled out systems for which at fixed secondary mass no tertiary mass could enable eclipses of the necessary depth (in $\mathrm{R_C}$-band, or in $\mathrm{B_J}$-band). The $\mathrm{R_C}$-band limit corresponded to a secondary mass limit of $M_2 > 0.27 M_\odot$, and the $\mathrm{B_J}$-band corresponded to a stronger limit of $M_2 > 0.70 M_\odot$.

Multicolor photometry and BEB scenarios —While the above constraints rule out HEBs, certain configurations of BEB systems (*e.g.*, a background G0V+K3V binary) can produce blue eclipses while remaining undetected along the line of sight. Such scenarios are constrained by the lack of an ob-

[3] http://svo2.cab.inta-csic.es/theory/fps/

served secondary eclipse, and therefore require either eccentric orbits to avoid secondary eclipses, or else a background twin binary system at double the orbital period. The only way to definitively rule out such scenarios is to prove that the loss of light is from the target star, for instance by detecting the Rossiter-McLaughlin effect during a transit, and confirming that the spectroscopic transit is consistent with the photometric transit.

3.1.6. *Gaia*

The "Gaia" curve in Figure 5 combines both point-source detections from imaging, and sources that show an astrometric excess. The curve was interpolated from Figure 4 of Rizzuto et al. (2018). TOI 837 has a RUWE statistic of 1.022, indicative that there are no obviously present astrometric companions. The UWE statistic (square-root of the reduced astrometric χ^2) is 1.38, which is consistent with stars of similar brightness and color (Lindegren et al. 2018, Appendix A).

3.1.7. *Patient Imaging*

Archival SERC-J and AAO-SES plates are available for the TOI 837 field[4]. These plates were acquired in 1982 and 1992, respectively. For high proper motion stars archival imagery can be used to detect slowly moving background stars that might be an astrophysical false-positive source (*e.g.*, Bakos et al. 2006; Huang et al. 2018b; Vanderburg et al. 2019). However TOI 837 has only moved $\approx 0.7''$ between 1982 and present, in comparison to the $\approx 2.0''$ FWHM of the target on the plates. We therefore cannot resolve it from background sources not already resolved through more modern imaging.

3.2. *False positive probability*

The constraints on false-positive scenarios summarized in Figure 5 rule out the possibilities that *i)* the eclipses are caused by a star orbiting TOI 837, *ii)* the eclipses are caused by hierarchical blends, and *iii)* the eclipses are caused by neighboring stars outside $\approx 2''$. The only scenario not formally ruled out is a background eclipsing binary. A simple (fallacious) argument on the a priori probability of background blends follows from counting statistics. The local density of $T < 15.1$ stars around TOI 837, found by counting from TIC8, is $3.7 \times 10^{-4}\,\mathrm{arcsec}^{-2}$. Therefore within the relevant $\approx 0.3''$ radius not excluded by the SOAR HRCam contrast curve, for a randomly selected star we would expect 1.0×10^{-4} potential $T < 15.1$ contaminants, which appears small.

The reason the above statement is an insufficient argument against BEBs is that TOI 837 is not a randomly selected star—it was selected because it shows eclipses. Given a foreground star that shows eclipses, the probability of a background star being present is much greater than for an arbitrary foreground star. The relevant populations need to be modeled at the Monte Carlo level. We opt to use `VESPA` to model the populations (Morton 2012, 2015b).

`VESPA` calculates the false positive probability for a transit signal as

$$\mathrm{FPP} = 1 - P_{\mathrm{pl}}, \tag{3}$$

where in our case the probability that the signal comes from a planet, P_{pl}, is given by

$$P_{\mathrm{pl}} = \frac{\mathcal{L}_{\mathrm{pl}}\pi_{\mathrm{pl}}}{\mathcal{L}_{\mathrm{pl}}\pi_{\mathrm{pl}} + \mathcal{L}_{\mathrm{BEB}}\pi_{\mathrm{BEB}}}, \tag{4}$$

where $\mathcal{L}_i$ is the model likelihood for the planet and BEB scenarios, and π_i is the model prior. The terms labeled as "BEB" usually include other false positive scenarios (HEBs and EBs), but our followup data have excluded these possibilities. The priors are evaluated using a combination of galactic population synthesis (Girardi et al. 2005), binary star statistics (Raghavan et al. 2010), and specific planet occurrence rates (Morton 2012, Section 3.4). The likelihoods are evaluated by forward-modeling a representative population of eclipsing bodies for model class, in which each population member has a particular trapezoidal eclipse depth, total duration, and ingress duration. The likelihood is then calculated by multiplying the probability distribution function of simulated population's shape parameters with the posterior probability of the actual observed eclipse shape.

We ran `VESPA`[5], and directly incorporated our constraints of the SOAR *I*-band contrast curve and a non-detection of secondary eclipses with a depth set at roughly twice the limits from the SPOC vetting report (0.1%). We verified that changing the secondary eclipse depth limit did not significantly affect the results. We set the maximum aperture radius at $2''$, based on our ground-based photometry. Incorporating the constraints from Figure 5, our nominal false positive probability analysis excluded EB and HEB scenarios. This yielded an FPP of 0.21% for TOI 837.01, sufficient for formal validation as a planet (Morton 2012). We did not incorporate our constraint that TOI 837 is not double-lined, which rules out an additional portion of BEB parameter space. Had we not acquired multicolor ground-based photometry, and been unable to exclude HEB scenarios, the FPP would have risen to 8%. Since the transits are achromatic (Figure 3), particularly in Johnson-B band, we can rule out HEB scenarios.

One potential caveat in our approach is that `VESPA` uses a galactic population synthesis to model the sight-line. Since TOI 837 is in the foreground of IC 2602 (see Section 4.2), for roughly 25 pc behind the sightline to the star, the number of background stars is higher than `VESPA` would predict due to the presence of the cluster. To quantify the importance of this effect, we assessed the sky-plane density of potential contaminants by counting stars brighter than $T = 15.07$ within 0.5 degrees of TOI 837 (Stassun et al. 2019). We then compared this density against sightlines rotated in galactic longitude towards and away from the galactic center. Within $\pm 10^\circ$ in galactic longitude, the sky-plane density of stars fluctuated at the level of $\approx 15\%$, with a local maximum a few degrees

[4] https://archive.stsci.edu/cgi-bin/dss_form

[5] We used `VESPA-0.6` and `isochrones-1.2.2`.

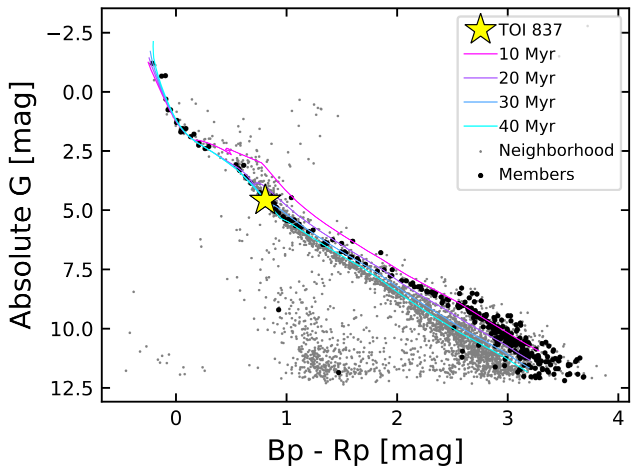

Figure 6. Hertzsprung-Russell diagram of TOI 837 and members of IC 2602. Members (black circles) were identified by Cantat-Gaudin et al. (2018). Gray circles are non-member stars within 5 standard deviations of the mean IC 2602 right ascension, declination, and parallax. G denotes Gaia broadband magnitudes, Bp Gaia blue, and Rp Gaia red. MIST isochrones (colored lines) fit the upper main sequence well, but diverge from the data for $M_\star \lesssim 0.7 M_\odot$. This is a known issue with the M dwarf models (see Section 4.1.2).

away from TOI 837, towards the center of IC 2602. The overall density also slowly increased towards the galactic center. We therefore do not expect this consideration to significantly alter our FPP calculation.

4. SYSTEM MODELING

4.1. *The Cluster*

4.1.1. *Physical Characteristics*

The IC 2602 cluster is about 150 pc from the Earth, and is near the galactic plane with $(l,b) \approx (289.6^\circ, -5.0^\circ)$ (Cantat-Gaudin et al. 2018). It is also sometimes called the θ Carinae cluster, after its brightest member, or also the "Southern Pleiades". While IC 2602 is close to the Lower Centaurus Crux subgroup of the Scorpio-Centaurus OB2 association in both position and proper motion space, its older age and clear kinematic separation indicate that it is a distinct stellar population (de Zeeuw et al. 1999; Damiani et al. 2019).

Reliable ages reported for IC 2602 range from 30–46 Myr. We have collected ages reported over the years in Table 3. The Li depletion boundary technique yields slightly older absolute ages than isochrone fitting (Dobbie et al. 2010; Randich et al. 2018). Rather than redetermine the age of the cluster and add another line to the table, we simply adopt an absolute age range for TOI 837 of 30–46 Myr.

Reported mean metallicity values [Fe/H] for the cluster range between slightly super-solar (0.04 ± 0.01, Baratella et al. 2020) and slightly sub-solar (-0.02 ± 0.02, Netopil et al. 2016). The extinction $E(B-V)$ is rather low, with reported values ranging from 0.03 to 0.07 (*e.g.*, Randich et al. 2018).

Table 3. Previously reported ages for the open cluster IC 2602.

Method	Age [Myr]	Reference
MSTO isochrone	36.3	Mermilliod (1981)
PMS+MSTO isochrone	30 ± 5	Stauffer et al. (1997)
Isochrone (a)	67.6	Kharchenko et al. (2005)
Isochrone (b)	221	Kharchenko et al. (2013)
Isochrone	67.6	van Leeuwen (2009)
LDB (c)	46^{+6}_{-5}	Dobbie et al. (2010)
MSTO isochrone (d)	$41-46$	David & Hillenbrand (2015)
MSTO isochrone (e)	$37-43$	David & Hillenbrand (2015)
Li selection + isochrone	$43.7^{+4.3}_{-3.9}$	Bravi et al. (2018)
Isochrone (f)	30^{+9}_{-7}	Randich et al. (2018)
LDB	$43.7^{+4.3}_{-3.9}$	Randich et al. (2018)
Isochrone	$35.5^{+0.8}_{-1.6}$	Bossini et al. (2019)
Isochrone	$35.5^{+14.6}_{-10.4}$	Kounkel & Covey (2019)

NOTE— MSTO ≡ main sequence turn-off. PMS ≡ pre-main-sequence. LDB ≡ lithium depletion boundary. (a) Based on location in HR diagram of just two stars. (b) Notes major age change since Kharchenko et al. (2005). (c) Dobbie et al. (2010) performed a dedicated study of the LDB in IC 2602. Comparing to early isochronal ages, they write their age is "consistent with the general trend delineated by the Pleiades, α-Per, IC 2391, and NGC 2457, whereby the LDB age is 120-160 per cent of the estimates derived using more traditional techniques" such as isochrone fitting. (d) Using Ekström et al. (2012) evolutionary models. (e) Using PARSEC evolutionary models (Bressan et al. 2012). (f) Averaged across PROSECCO, PARSEC, MIST models in (J, H, K_s) and (J, H, K_s, V) planes.

Kinematically, IC 2602 seems to be supervirial, in the sense that the observed stellar velocity dispersion is larger than the value expected if it were in virial equilibrium by about a factor of two (Bravi et al. 2018). Damiani et al. (2019) also reported evidence for the ongoing evaporation of IC 2602, in the form of a diffuse $\approx 10^\circ$ halo of young stars around the central density cusps. A gyrochronological study of these stars could confirm that these stars are truly coeval with the cluster.

4.1.2. *HR Diagram*

Figure 6 shows a Hertzsprung-Russell diagram of TOI 837, the IC 2602 cluster, and the "neighborhood" of spatially nearby stars. Stars labeled as "cluster members" are those reported by Cantat-Gaudin et al. (2018) based on Gaia DR2 positions, proper motions, and parallaxes. We included candidate members with formal membership probability exceeding 10%. Most members appear to be young and coeval. TOI 837 is in its expected position relative to the other members along the cluster isochrone. This photometrically limits the presence of binary companions in the TOI 837 system, to within perhaps half the brightness (≈ 0.75 magnitudes) of the target star.

Figure 6 suggests that the membership census of IC 2602 is incomplete. We defined the reference "neighborhood" as the group of at most 10^4 randomly selected non-member stars within 5 standard deviations of the mean IC 2602 right ascension, declination, and parallax. We queried Gaia DR2 for these stars using `astroquery` (Ginsburg et al. 2018). Many low-mass stars appear above the main sequence, even though they were not identified as 5-dimensional kinematic members through the unsupervised Cantat-Gaudin et al. (2018) membership assignment process.

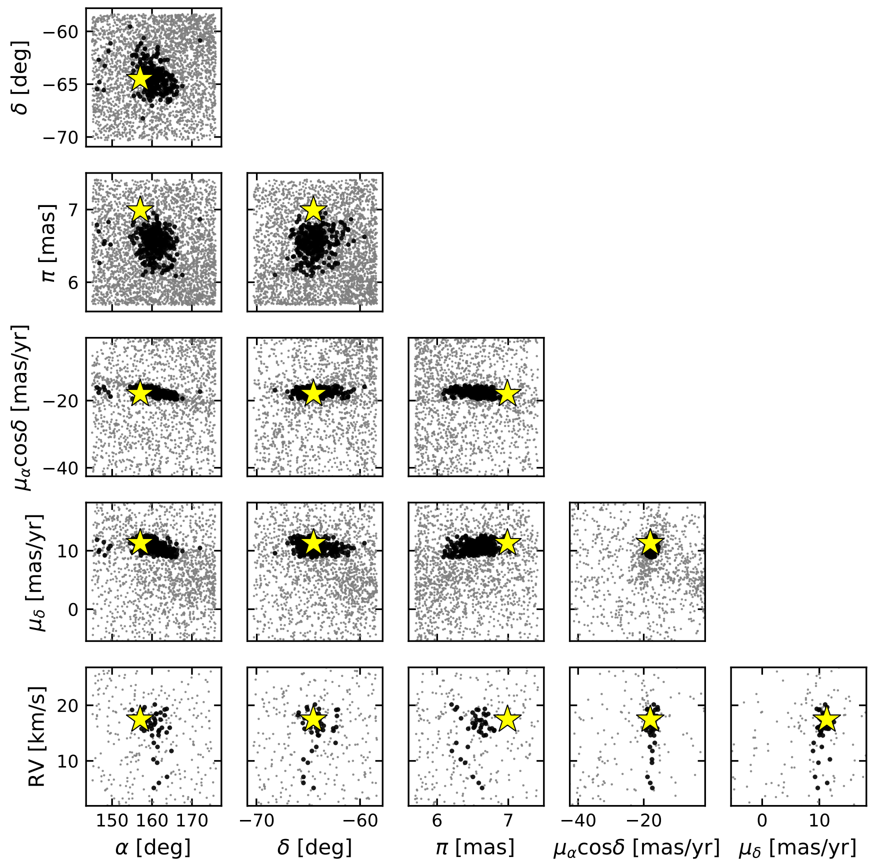

Figure 7. Positions and kinematics of TOI 837 (star), IC 2602 members (black circles), and stars in the neighborhood (gray circles). Members were identified by Cantat-Gaudin et al. (2018). α denotes right ascension, δ declination, π parallax, μ_δ and μ_α proper motion in each equatorial direction, and RV radial velocity reported by Gaia DR2. The RVs are for unblended spectra of bright stars ($G \lesssim 12$). The proper motion projection (μ_δ vs. $\mu_\alpha \cos\delta$) highlights incompleteness in the membership selection function.

Figure 6 also compares the data to the MIST isochrones (Choi et al. 2016). We used the web-interace[6] to interpolate isochrones at 10, 20, 30, and 40 million years. We assumed solar metallicity, and a fixed extinction value of $A_V = 0.217$ (Randich et al. 2018). The 30 and 40 Myr models align well with the data for stars with masses ranging from roughly 0.7–$7\,M_\odot$. The PMS K and M dwarf models are bluer than observed in the Gaia photometry. This discrepancy was noted and discussed at length by Choi et al. (2016). One suggested explanation was that strong magnetic fields in low-mass pre-main-sequence stars inhibit convection and produce a high filling factor of starspots (*e.g.*, Stauffer et al. 2003; Feiden & Chaboyer 2013). This explanation however fails to explain poor isochrone fits in both old open clusters (*e.g.*, M67) and the field, particularly in blue bandpasses. An alternative explanation is that the molecular line lists for M dwarf atmospheres are incomplete in these wavelength ranges (Rajpurohit et al. 2013; Mann et al. 2013).

4.2. *The Star*

4.2.1. *Membership of TOI 837 in IC 2602*

TOI 837 has been reported as a member of IC 2602 by many independent investigators (*e.g.*, Kharchenko et al. 2013; Oh et al. 2017; Cantat-Gaudin et al. 2018; Damiani et al. 2019; Kounkel & Covey 2019). The simplest way to verify the membership is through inspection of the Gaia DR2 position and kinematics. Figure 7 shows the six-dimensional positions and kinematics of TOI 837, IC 2602 members, and nearby stars. The "neighborhood" is defined as in Figure 6. The axes limits for the right ascension, declination, and parallax dimensions are set by being within 5 standard deviations of the mean IC 2602 right ascension, declination, and parallax. The axes limits for the proper motion and radial velocity dimensions are set at the 25$^{\text{th}}$ and 75$^{\text{th}}$ percentiles, in order to give a sense of the population's distribution, while excluding outliers. The radial velocities suffer the greatest incompleteness due to the current $G \approx 12$ magnitude limit of the Gaia DR2 data processing.

Figure 7 provides strong evidence that TOI 837 is a member of IC 2602. The only dimension that could lead to some worry is the parallax, as TOI 837 is one of the closest IC 2602 members reported by Cantat-Gaudin et al. (2018). Fortu-

[6] http://waps.cfa.harvard.edu/MIST/interp_isos.html, 2020-07-08

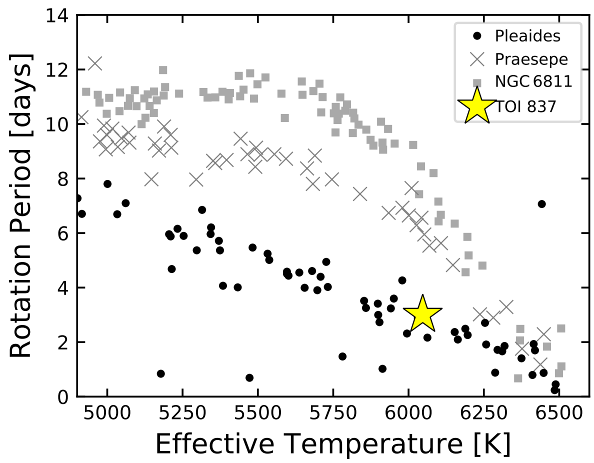

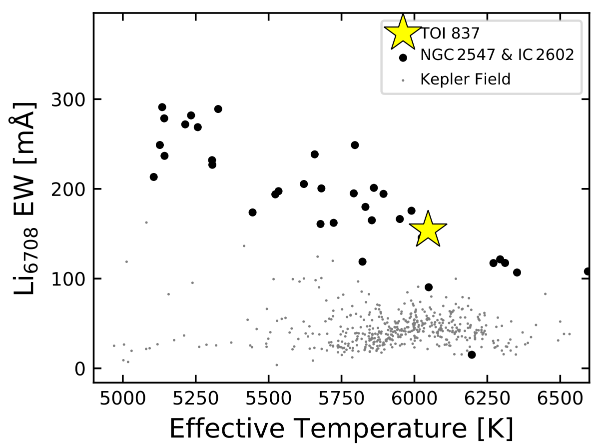

Figure 8. Youth diagnostics. *Top:* Rotation periods for TOI 837 and selected open clusters. The Pleiades (120 Myr), Praesepe (670 Myr), and NGC 6811 (1000 Myr) are shown. Their rotation periods were measured by Rebull et al. (2016); Douglas et al. (2017, 2019), and Curtis et al. (2019a), respectively. *Bottom:* Lithium 6708Å equivalent widths for TOI 837, field stars, and young open clusters. The field star sample is drawn from Kepler planet hosts, and was measured by Berger et al. (2018) using Keck-HIRES. The young open clusters members were surveyed by Randich et al. (2018) using the UVES and GIRAFFE spectrographs at the ESO VLT. Randich et al. (2018) found lithium depletion boundary ages for these clusters of $37.7^{+5.7}_{-4.8}$ Myr (NGC 2547) and $43.7^{+4.3}_{-3.9}$ Myr (IC 2602).

nately, there are independent means of verifying the star's youth.

4.2.2. *Rotation*

As stars get older, their rotation rates incrementally slow due to magnetic braking Weber & Davis (1967); Skumanich (1972). One way to verify the youth of TOI 837 is by comparing its rotation period to other stars with known ages.

We measured the rotation period from the TESS `PDCSAP` light curve using the Lomb-Scargle periodogram implemented in `astropy` (Lomb 1976; Scargle 1982; VanderPlas & Ivezić 2015). We fitted the light curve without masking out the transits or flares, as these represent a small fraction of the overall time series. To derive the uncertainty on the best period, we fitted a Gaussian to the dominant peak, after first ensuring that we had oversampled the initial frequency grid. This gave a rotation period of $P_{\rm rot} = 2.987 \pm 0.056$ d when allowing for a single Fourier terms in the periodogram model, and $P_{\rm rot} = 3.004 \pm 0.053$ d when allowing for two Fourier terms. As the second model provides a better fit to the data, we adopt the second measurement.

As we will discuss in Section 4.2.4, we measured the star's radius by combining the spectroscopic effective temperature with a broadband photometry SED fit. We would expect, combining our $R_\star$ and $P_{\rm rot}$ measurements, that the equatorial velocity v of the star would be $17.67 \pm 0.32\,{\rm km\,s^{-1}}$. Our spectroscopically measured $v \sin i$ from CHIRON, $16.2 \pm 1.1\,{\rm km\,s^{-1}}$ agrees reasonably well with this expectation.

The star is clearly a rapid rotator. Figure 8 compares its rotation period with rotation periods that have been measured in a number of well-studied open clusters. TOI 837 seems to be gyrochronologically coeval with the Pleiades sequence. This is not to say that TOI 837 is "Pleiades-aged", because the observed scatter in the rotation-period diagram for the first 10–100 Myr is quite high (see Figure 9 of Rebull et al. 2020). Instead, we interpret the rotation period as evidence to support the claim that TOI 837 is younger than ~ 500 Myr.

4.2.3. *Lithium*

Lithium depletion for early G-dwarfs like TOI 837 requires hundreds of megayears (Soderblom et al. 2014). This is because their convective envelopes are shallow, and so transport of photospheric lithium to the hot core takes place over diffusive timescales, rather than convective timescales. Nonetheless, comparison of early G-dwarfs in the field to *e.g.*, 600 Myr old Hyads has shown that the depletion does indeed happen over many gigayears (Berger et al. 2018).

The spectra of TOI 837 all show the 6708 Å lithium doublet in absorption. Opting to use our FEROS spectra because of their high S/N, we measured the line's equivalent width (EW) to be 154 ± 9 mÅ. Figure 8 compares this EW to stars in the field, and other young open cluster members. The field star measurements were collected by Berger et al. (2018); we show their reported lithium detections with $S/N > 3$. The young open cluster members were selected for the presence of lithium, as described by Randich et al. (2018). The measured TOI 837 Li EW is much larger than observed for field stars, and is consistent with lithium absorption seen in stars with similar colors in sub-100 Myr moving groups.

4.2.4. *Stellar Parameters*

Select properties of TOI 837 from the literature and our analysis are presented in Table 4. We calculated the stellar parameters using two different approaches.

In "Method 1", we measured spectroscopic parameters from each of the CHIRON spectra (Section 2.5.1). We then calculated the stellar radius and reddening following Stassun

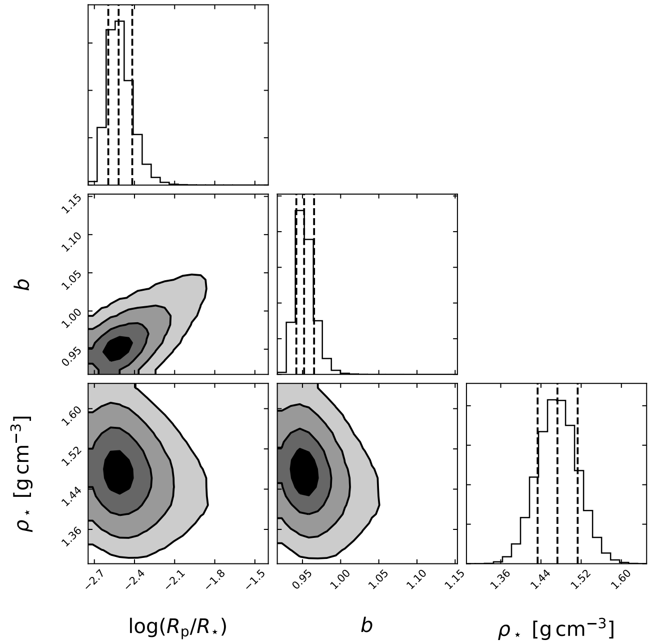

Figure 9. Posterior probabilities of impact parameter, planet-to-star size ratio, and stellar density. Contours are shown at 1, 2, 3, and 4-σ confidence. The planet-to-star size ratio corresponds to a planet size between $0.68 R_{\rm Jup}$ and $0.97 R_{\rm Jup}$ ($3^{\rm rd}$–$97^{\rm th}$ percentile). This plot was made using `corner` (Foreman-Mackey 2016).

et al. (2017). We first derived the bolometric flux by combining available broadband magnitudes from Gaia, Tycho-2, APASS, 2MASS, and WISE. We then fitted the SED with the Kurucz (2013) stellar atmopshere models, and summed to find $F_{\rm bol}$. When fitting the atmosphere model, we varied the extinction ($A_{\rm V}$) and the overall normalization. This procedure yielded $A_{\rm V} = 0.20 \pm 0.03$, which agrees with the average from the IC 2602 isochrone fits of Randich et al. (2018). Combining the spectroscopic effective temperature, bolometric flux, and Gaia distance, we determined the stellar radius using the Stefan-Boltzmann law. Combining this radius with the spectroscopic $\log g$ also yields a stellar mass.

In "Method 2", we simply used the observed location of TOI 837 in the HR diagram and interpolated against the 40 Myr isochrone. This method leverages the relative location of TOI 837 within the narrow IC 2602 isochrone to derive precise, theoretically self-consistent constraints on all of the stellar parameters. Although this approach would fail for a low-mass star, TOI 837 is above the stellar masses where the Gaia photometry and isochrone models begin to diverge.

Method 1 yielded a stellar mass that seemed to be high relative to the observed CHIRON effective temperature ($1.21 M_\odot$ to 5946 K, with relative uncertainties of a few percent on each). To avoid poorly understood systematics, we adopted the stellar parameters from Method 2, and report them in Table 4.

4.3. *The Planet*

We also fitted the available time-series photometry of TOI 837.01 using two different approaches. To derive the most precise possible ephemeris, we fitted the ground and space-based transits simultaneously. To derive the physical parameters of the planet, we fitted the TESS data alone, due to our better understanding of the underlying systematic trends and the higher precision.

For the TESS `PDCSAP` light curve, we first eliminated points that had quality flags corresponding to any of bits $\{3,4,6,8,11,12\}$. This excluded cadences affected by coarse spacecraft pointing, reaction wheel desaturation events, manual flags, cosmic ray hits, and straylight from the Earth or Moon being present. Inspecting the data, we also manually excluded the two flares shown in Figure 1. We then trimmed the TESS data to windows of ± 7 hr centered on each transit.

Our model for time-series photometry data was an Agol et al. (2019) transit with physical and orbital parameters shared across all transit windows, plus a local quadratic trend allowed within each window. Select parameters and priors are listed in Table 5, for the TESS-only model. In brief, we fitted for the shared stellar parameters $\{\log g, R_\star, u_0, u_1\}$, and the shared planetary parameters $\{t_0, P, b, \log(R_{\rm p}/R_\star)\}$. There were also three free trend parameters for each transit window to account for the local rotational variability. In the TESS-only model this yielded 23 free parameters, of which 8 were physically relevant and 15 were nuisance parameters. In the combined TESS and ground-based model, there were an additional 7 transits, and therefore an additional 21 nuisance parameters for a total of 44 free parameters.

We fitted the model using `PyMC3` (Salvatier et al. 2016; Theano Development Team 2016). For the exoplanet transit, we used the `exoplanet` code (Foreman-Mackey et al. 2020). After initializing each model with the parameters of the maximum *a posteriori* model, we assumed a Gaussian likelihood, and sampled using `PyMC3`'s gradient-based No-U-Turn Sampler (Hoffman & Gelman 2014). We used $\hat{R}$ as our convergence diagnostic (Gelman & Rubin 1992).

We opted for this approach rather than a joint fit of the photometry and radial velocities because the RVs on their own did not show evidence for a planetary signal. Our preference for using only the TESS data to derive the transit parameters was in our view justified by the systematic uncertainties inherent to ground-based light curve production, particularly in comparison star selection. Our assumption of a constant radius across all bandpasses was tested by independently fitting each ground-based transit while letting the planetary radius float (Section 3.1.5). The transit depths did not significantly change between different bandpasses.

The posteriors from fitting the TESS data alone are given in Table 5. The condition for a grazing transit is whether the impact parameter b is below $1 - R_{\rm p}/R_\star$. The transit is therefore either grazing, or nearly grazing. The relevant posterior probabilities are shown in Figure 9. From experimenting with the priors, we found that in the absence of a strong prior on the stellar density, the inherent degeneracy between the impact parameter and planet-to-star size ratio would have been much stronger. In the absence of precise information about the star,

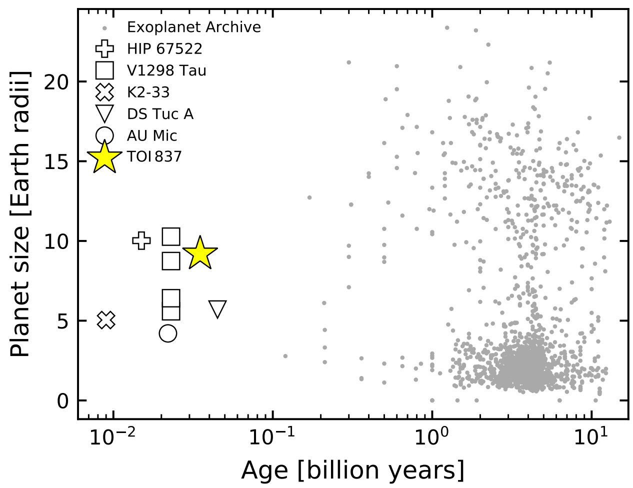

Figure 10. Planet radii versus ages, for the known transiting planets. Systems younger than 100 Myr are emphasized. Ages and radii are from the NASA Exoplanet Archive on 13 July 2020. Precise ages are known for only a small fraction of the gray points.

a larger fraction of the posterior would therefore have been grazing. However, our priors on the stellar parameters from the cluster isochrone fit break this degeneracy, enabling us to report two-sided limits on the planet-to-star size ratio.

5. DISCUSSION

TOI 837 joins a number of other young planetary systems reported from TESS, including DS Tuc Ab, HIP 67522b, TOI 1726, and AU Mic b (Newton et al. 2019; Zhou et al. 2019; Montet et al. 2019; Rizzuto et al. 2020; Mann et al. 2020; Plavchan et al. 2020; Palle et al. 2020; Addison et al. 2020; Martioli et al. 2020; Hirano et al. 2020). Figure 10 shows TOI 837 in the space of planet sizes and ages. TOI 837 is among the youngest transiting planets known. While we have statistically validated that TOI 837 is a planet, the possibility that it is a background eclipsing binary has not been excluded with sufficient confidence to call the planet "confirmed".

The easiest path towards definitively confirming whether TOI 837 is a planet will be a Rossiter-McLaughlin (RM) measurement. Detection of an RM signal consistent with the photometric transit would rule out BEB and HEB scenarios, as it would imply that the eclipsing object is bound to the target star. Combined with our non-detection of the planet's mass from radial velocity monitoring, this would confirm that TOI 837.01 is a planet.

The maximum amplitude of the Rossiter-McLaughlin anomaly is (Gaudi & Winn 2007)

$$\Delta V_{\rm RM} \approx f_{\rm LD} \cdot \delta \cdot v \sin i \cdot \sqrt{1-b^2} \approx 14\,{\rm m\,s^{-1}}, \tag{5}$$

for

$$f_{\rm LD} = 1 - c_1(1-\mu) - c_2(1-\mu)^2, \tag{6}$$

where $\mu \approx (1-b^2)^{1/2}$, and for calculation purposes we assumed $b = 0.95$ and used stellar and transit parameters from Tables 4 and 5. Although challenging, for a 1.9 hr transit of a $V = 10.6$ star, a detection could be achieved with modern spectrographs. The next viable total transit windows from Chile occur in January and February of 2021; there are also a few visible per season from other southern locations. The most precise available ephemeris, found from our joint fit of the TESS and ground-based photometry, is as follows.

$$\begin{aligned} t_0\ [\mathrm{BJD_{TDB}}] &= 2458574.272523 \pm 0.000594 \\ P\ [\mathrm{d}] &= 8.3248762 \pm 0.0000156 \\ T_{14}\ [\mathrm{hr}] &= 1.86 \pm 0.04. \end{aligned} \tag{7}$$

The Rossiter-McLaughlin approach is more likely to yield short-term success than a direct mass measurement because of the RV noise expected to be induced by stellar rotation. The photometric amplitude induced by starspots on TOI 837 is $\approx 2\%$. The spot-induced RV variation expected over the course of the ≈ 3 d rotation period can then be estimated by multiplying the photometric amplitude and spectroscopic equatorial velocity. This gives $\sigma_{\rm RV,rot} \approx 300\,{\rm m\,s^{-1}}$, and is consistent with the scatter we observe in our radial velocities from FEROS. Detecting a planet's Doppler signal in these regimes is challenging, and requires a significant amount of data and care in signal extraction (Barragán et al. 2019). The Rossiter-McLaughlin measurement avoids the majority of this issue because the transit occurs over a much shorter duration than a single stellar rotation period.

If the RM measurements prove that the validated planet is real, a campaign to measure the mass timed to coincide with TESS sectors 36 and 37 (late March to late May of 2021) would significantly ease the extraction of the planetary Doppler signal. The reason is that the RVs, activity indicators, and photometry could be modeled simultaneously (*e.g.*, Rajpaul et al. 2015). This would greatly constrain models of the spot-induced RV signal. The mass measurement would likely be worthwhile in order to improve understanding of the planet's contraction and photoevaporation history.

While we hope that RV observations will be pursued, data acquired during the first TESS mission extension may also help in understanding the system (Bouma et al. 2017; Huang et al. 2018a). Any misalignment between the star's spin axis and the planet's orbit should induce nodal precession, which could yield large changes in the transit duration given the system's high impact parameter. If observed, this could be a spectroscopy-free method for confirming the planet.

ACKNOWLEDGMENTS

This paper includes data collected by the TESS mission, which are publicly available from the Mikulski Archive for Space Telescopes (MAST). Funding for the TESS mission is provided by NASA's Science Mission directorate. TOI 837 was included on the TESS 2-minute target list in part thanks to the Guest Investigator program of G. Sacco (G011265).

We acknowledge support from the French and Italian Polar Agencies, IPEV and PNRA, and from Université Côte d'Azur under Idex UCAJEDI (ANR-15-IDEX-01). We thank the dedicated staff at Concordia for their continuous presence and support throughout the Austral winter. This research received funding from the European Research Council (ERC) under the European Union's Horizon 2020 research and innovation programme (grant agreement n° 803193/BEBOP), and from the Science and Technology Facilities Council (STFC; grant n° ST/S00193X/1).

This research made use of the Exoplanet Follow-up Observation Program website, which is operated by the California Institute of Technology, under contract with the National Aeronautics and Space Administration under the Exoplanet Exploration Program. This research made use of the NASA Exoplanet Archive, which is operated by the California Institute of Technology, under contract with the National Aeronautics and Space Administration under the Exoplanet Exploration Program.

This research made use of the SVO Filter Profile Service (http://svo2.cab.inta-csic.es/theory/fps/) supported from the Spanish MINECO through grant AYA2017-84089.

Resources supporting this work were provided by the NASA High-End Computing (HEC) Program through the NASA Advanced Supercomputing (NAS) Division at Ames Research Center for the production of the SPOC data products.

A.J. and R.B. acknowledge support from project IC120009 "Millennium Institute of Astrophysics (MAS)" of the Millenium Science Initiative, Chilean Ministry of Economy. A.J. acknowledges additional support from FONDECYT project 1171208. J.I.V acknowledges support from CONICYT-PFCHA/Doctorado Nacional-21191829. R.B. acknowledges support from FONDECYT Post-doctoral Fellowship Project 3180246. C.Z. is supported by a Dunlap Fellowship at the Dunlap Institute for Astronomy & Astrophysics, funded through an endowment established by the Dunlap family and the University of Toronto.

Software: `astrobase` (Bhatti et al. 2018), `AstroImageJ` (Collins et al. 2017), `astropy` (Astropy Collaboration et al. 2018), `astroquery` (Ginsburg et al. 2018), `ceres` (Brahm et al. 2017), `cdips-pipeline` (Bhatti et al. 2019), `corner` (Foreman-Mackey 2016), `exoplanet` (Agol et al. 2019) `exoplanet` (Foreman-Mackey et al. 2020), and its dependencies (Agol et al. 2019; Kipping 2013; Luger et al. 2019; Theano Development Team 2016), `IDL Astronomy User's Library` (Landsman 1995), `IPython` (Pérez & Granger 2007), `isochrones` (Morton 2015a), `lightkurve` (Lightkurve Collaboration et al. 2018), `matplotlib` (Hunter 2007), `MESA` (Paxton et al. 2011, 2013, 2015) `numpy` (Walt et al. 2011), `pandas` (McKinney 2010), `pyGAM` (Servén et al. 2018), `PyMC3` (Salvatier et al. 2016), `radvel` (Fulton et al. 2018), `scipy` (Jones et al. 2001), `tesscut` (Brasseur et al. 2019), `VESPA` (Morton 2012, 2015b), `webplotdigitzer` (Rohatgi 2019), `wotan` (Hippke et al. 2019).

Facilities: *Astrometry*: Gaia (Gaia Collaboration et al. 2016, 2018). *Imaging*: Second Generation Digitized Sky Survey, SOAR (HRCam; Tokovinin 2018). *Spectroscopy*: CTIO1.5 m (CHIRON; Tokovinin et al. 2013), MPG2.2 m (FEROS; Kaufer et al. 1999), AAT (Veloce; Gilbert et al. 2018). *Photometry*: ASTEP:0.40 m (ASTEP400), El Sauce:0.356 m, TESS (Ricker et al. 2015).

Table 4. Literature and Measured Properties for TOI 837

Parameter	Description	Value	Source
Other identifiers			
	TIC 460205581		
	GAIADR2 5251470948229949568		
$\alpha_{J2015.5}$	Right Ascension (hh:mm:ss)	10:28:08.95	1
$\delta_{J2015.5}$	Declination (dd:mm:ss)	-64:30:18.76	1
$l_{J2015.5}$	Galactic Longitude (deg)	288.2644	1
$b_{J2015.5}$	Galactic Latitude (deg)	-5.7950	1
B	Johnson B mag.	11.119 ± 0.107	2
V	Johnson V mag.	10.635 ± 0.020	2
G	Gaia G mag.	10.356 ± 0.020	1
Bp	Gaia Bp mag.	10.695 ± 0.020	1
Rp	Gaia Rp mag.	9.887 ± 0.020	1
T	TESS mag.	9.9322 ± 0.006	2
J	2MASS J mag.	9.392 ± 0.030	3
H	2MASS H mag.	9.108 ± 0.038	3
K_S	2MASS K_S mag.	8.933 ± 0.026	3
W1	WISE1 mag.	8.901 ± 0.023	4
W2	WISE2 mag.	8.875 ± 0.021	4
W3	WISE3 mag.	8.875 ± 0.020	4
W4	WISE4 mag.	$8.936 \pm$ N/A	4
π	Gaia DR2 parallax (mas)	6.989 ± 0.022	1
d	Distance (pc)	143.1 ± 0.5	1
μ_α	Gaia DR2 proper motion in RA (mas yr^{-1})	-18.017 ± 0.039	1
μ_δ	Gaia DR2 proper motion in DEC (mas yr^{-1})	11.307 ± 0.037	1
RV	Systemic radial velocity (km s^{-1})	$17.44 \pm 0.64^{\dagger}$	1
$v \sin i_\star$	Rotational velocity (km s^{-1})	16.2 ± 1.1	5
$v_{\rm Mac}$	Macroturbulence velocity (km s^{-1})	8.4 ± 2.9	5
[Fe/H]	Metallicity	-0.069 ± 0.042	5
$T_{\rm eff}$	Effective Temperature (K)	6047 ± 40	6
$\log g_\star$	Surface Gravity (cgs)	4.467 ± 0.010	6
Li EW	6708Å Equiv. Width (mÅ)	154 ± 9	7
$P_{\rm rot}$	Rotation period (d)	3.004 ± 0.053	8
Age	Adopted stellar age (Myr)	30–46	9
Spec. Type	Spectral Type	G0/F9 V	5
$R_\star$	Stellar radius ($R_\odot$)	1.022 ± 0.015	6
$M_\star$	Stellar mass ($R_\odot$)	1.118 ± 0.011	6
$A_{\rm V}$	Interstellar reddening (mag)	0.20 ± 0.03	10

NOTE— † Systemic RV uncertainty is the standard deviation of single-transit radial velocities, as quoted in Gaia DR2. Provenances are: [1]Gaia Collaboration et al. (2018), [2]Stassun et al. (2019), [3]Skrutskie et al. (2006), [4]Wright et al. (2010), [5]CHIRON spectra, [6]Method 2 (cluster isochrone, Section 4.2.4), [7]FEROS spectra, [8]TESS light curve, [9]IC 2602 ages from isochrone & lithium depletion analyses (Section 4.1.1), [10]Method 1 (photometric SED fit, Section 4.2.4).

Table 5. Priors and posteriors for the model fitted to the TESS data.

Param.	Unit	Prior	Median	Mean	Std. Dev.	3%	97%
Sampled							
P	d	$\mathcal{N}(8.3249; 0.1000)$	8.3247158	8.3247141	0.0003210	8.3240946	8.3253007
$t_0^{(1)}$	d	$\mathcal{N}(1574.273800; 0.1000)$	1574.2730012	1574.2730125	0.0010420	1574.2710233	1574.2749496
$\log R_p/R_\star$	–	$\mathcal{U}(-4.605; 0.000)$	-2.51877	-2.50605	0.09466	-2.66494	-2.32807
b	–	$\mathcal{U}(0; 1+R_p/R_\star)$	0.9521	0.9536	0.0125	0.9318	0.9768
u_1	–	$\mathcal{U}(0.175; 0.475)^{(2)}$	0.335	0.332	0.086	0.196	0.475
u_2	–	$\mathcal{U}(0.085; 0.385)^{(2)}$	0.243	0.240	0.086	0.105	0.384
$R_\star$	$R_\odot$	$\mathcal{T}(1.022; 0.015)$	1.022	1.022	0.015	0.994	1.050
$\log g$	cgs	$\mathcal{N}(4.467; 0.010)$	4.467	4.467	0.010	4.448	4.486
$a_{00;\mathrm{TESS}}$	–	$\mathcal{N}(1.00; 0.01)$	0.9985	0.9985	0.0001	0.9983	0.9986
$a_{01;\mathrm{TESS}}$	d^{-1}	$\mathcal{U}(-0.05; 0.05)$	-0.0004	-0.0004	0.0003	-0.0011	0.0002
$a_{02;\mathrm{TESS}}$	d^{-2}	$\mathcal{U}(-0.05; 0.05)$	-0.0168	-0.0168	0.0023	-0.0211	-0.0124
$a_{10;\mathrm{TESS}}$	–	$\mathcal{N}(1.00; 0.01)$	1.0089	1.0089	0.0001	1.0088	1.0091
$a_{11;\mathrm{TESS}}$	d^{-1}	$\mathcal{U}(-0.05; 0.05)$	-0.0138	-0.0138	0.0003	-0.0144	-0.0132
$a_{12;\mathrm{TESS}}$	d^{-2}	$\mathcal{U}(-0.05; 0.05)$	-0.0536	-0.0536	0.0022	-0.0577	-0.0494
$a_{20;\mathrm{TESS}}$	–	$\mathcal{N}(1.00; 0.01)$	0.9991	0.9991	0.0001	0.9989	0.9993
$a_{21;\mathrm{TESS}}$	d^{-1}	$\mathcal{U}(-0.05; 0.05)$	0.0156	0.0156	0.0004	0.0150	0.0163
$a_{22;\mathrm{TESS}}$	d^{-2}	$\mathcal{U}(-0.05; 0.05)$	0.0246	0.0246	0.0024	0.02	0.0289
$a_{30;\mathrm{TESS}}$	–	$\mathcal{N}(1.00; 0.01)$	1.0012	1.0012	0.0001	1.0010	1.0014
$a_{31;\mathrm{TESS}}$	d^{-1}	$\mathcal{U}(-0.05; 0.05)$	0.0021	0.0021	0.0004	0.0014	0.0029
$a_{32;\mathrm{TESS}}$	d^{-2}	$\mathcal{U}(-0.05; 0.05)$	-0.0079	-0.0079	0.0029	-0.0133	-0.0025
$a_{40;\mathrm{TESS}}$	–	$\mathcal{N}(1.00; 0.01)$	0.9906	0.9906	0.0001	0.9904	0.9907
$a_{41;\mathrm{TESS}}$	d^{-1}	$\mathcal{U}(-0.05; 0.05)$	0.0015	0.0015	0.0003	0.0009	0.0022
$a_{42;\mathrm{TESS}}$	d^{-2}	$\mathcal{U}(-0.05; 0.05)$	0.0327	0.0327	0.0023	0.0283	0.0370
Derived							
$R_p/R_\star$	–	–	0.08	0.08	0.01	0.07	0.10
$\rho_\star$	g cm^{-3}	–	1.47	1.47	0.04	1.40	1.55
R_p	R_{Jup}	–	0.80	0.82	0.08	0.68	0.97
$a/R_\star$	–	–	17.54	17.54	0.16	17.24	17.84
$\cos i$	–	–	0.05	0.05	0.	0.05	0.06
T_{14}	hr	–	1.85	1.86	0.04	1.78	1.93
T_{13}	hr	–	0.20	0.21	0.10	0.01	NaN$^{(3)}$

NOTE— (1) For the most precise ephemeris based on the combination of TESS and ground-based data, please see Equation 7; the period and epoch are noted in this table only for self-consistency. (2) Assuming an informative quadratic limb-darkening prior with values about those given for the appropriate T_{eff} and $\log g$ in TESS-band from Claret (2017). The precision achieved in the ground-based data did not appear to necessitate using bandpass-dependent limb-darkening coefficients. (3) The second and third contact points do not exist for a grazing transit. *Notation*: $a_{ij;\mathrm{Instr}}$ denotes the i^{th} transit of a particular instrument, and the j^{th} polynomial detrending order. $\mathcal{U}$ denotes a uniform distribution, $\mathcal{N}$ a normal distribution, and $\mathcal{T}$ a truncated normal bounded between zero and an upper limit much larger than the mean.

REFERENCES

Abe, L., Gonçalves, I., Agabi, A., et al. 2013, A&A, 553, A49

Addison, B. C., Horner, J., Wittenmyer, R. A., et al. 2020, arXiv:2006.13675 [astro-ph], arXiv: 2006.13675

Agol, E., Luger, R., & Foreman-Mackey, D. 2019, arXiv e-prints, 1908.03222

Aigrain, S., Hodgkin, S., Irwin, J., et al. 2007, MNRAS, 375, 29

Angus, R., Aigrain, S., Foreman-Mackey, D., & McQuillan, A. 2015, MNRAS, 450, 1787, arXiv: 1502.06965

Astropy Collaboration, Price-Whelan, A. M., Sipőcz, B. M., et al. 2018, AJ, 156, 123

Bakos, G. A., Pál, A., Latham, D. W., Noyes, R. W., & Stefanik, R. P. 2006, ApJL, 641, L57

Baraffe, I., Chabrier, G., Barman, T. S., Allard, F., & Hauschildt, P. H. 2003, A&A, 402, 701

Baratella, M., D'Orazi, V., Carraro, G., et al. 2020, A&A, 634, A34

Barnes, S. A., Weingrill, J., Granzer, T., Spada, F., & Strassmeier, K. G. 2015, Astronomy & Astrophysics, 583, A73, arXiv: 1511.00554

Barragán, O., Aigrain, S., Kubyshkina, D., et al. 2019, MNRAS

Berger, T. A., Howard, A. W., & Boesgaard, A. M. 2018, ApJ, 855, 115

Berger, T. A., Huber, D., Gaidos, E., van Saders, J. L., & Weiss, L. M. 2020, arXiv e-prints, 2005

Bhatti, W., Bouma, L., & Yee, S. 2019, `cdips-pipeline v0.1.0`, https://doi.org/10.5281/zenodo.3370324

Bhatti, W., Bouma, L. G., & Wallace, J. 2018, `astrobase`, https://doi.org/10.5281/zenodo.1469822

Biddle, L. I., Johns-Krull, C. M., Llama, J., Prato, L., & Skiff, B. A. 2018, ApJL, 853, L34

Borucki, W. J., Koch, D., Basri, G., et al. 2010, Science, 327, 977

Bossini, D., Vallenari, A., Bragaglia, A., et al. 2019, A&A, 623, A108

Bouma, L. G., Hartman, J. D., Bhatti, W., Winn, J. N., & Bakos, G. Á. 2019, ApJS, 245, 13

Bouma, L. G., Winn, J. N., Kosiarek, J., & McCullough, P. R. 2017, arXiv:1705.08891 [astro-ph], arXiv: 1705.08891

Brahm, R., Jordán, A., & Espinoza, N. 2017, PASP, 129, 034002

Brahm, R., Espinoza, N., Jordán, A., et al. 2019, AJ, 158, 45

Brasseur, C. E., Phillip, C., Fleming, S. W., Mullally, S. E., & White, R. L. 2019, Astrophysics Source Code Library, ascl:1905.007

Bravi, L., Zari, E., Sacco, G. G., et al. 2018, A&A, 615, A37

Bressan, A., Marigo, P., Girardi, L., et al. 2012, MNRAS, 427, 127

Brucalassi, A., Koppenhoefer, J., Saglia, R., et al. 2017, A&A, 603, A85

Buchhave, L. A., Bakos, G. A., Hartman, J. D., et al. 2010, The Astrophysical Journal, 720, 1118

Burke, C. J., Gaudi, B. S., DePoy, D. L., & Pogge, R. W. 2006, AJ, 132, 210

Cameron, A. G. W., & Ward, W. R. 1976, 7, Conference Name: Lunar and Planetary Science Conference

Cantat-Gaudin, T., Jordi, C., Vallenari, A., et al. 2018, Astronomy & Astrophysics, 618, A93

Canup, R. M., & Asphaug, E. 2001, Nature, 412, 708

Castelli, F., & Kurucz, R. L. 2004, ArXiv Astrophysics e-prints, astro-ph/0405087

Chatterjee, S., Ford, E. B., Matsumura, S., & Rasio, F. A. 2008, ApJ, 686, 580

Choi, J., Dotter, A., Conroy, C., et al. 2016, ApJ, 823, 102

Ciardi, D. R., Crossfield, I. J. M., Feinstein, A. D., et al. 2018, AJ, 155, 10

Claret, A. 2017, Astronomy & Astrophysics, 600, A30, arXiv: 1804.10295

Collins, K. A., Kielkopf, J. F., Stassun, K. G., & Hessman, F. V. 2017, AJ, 153, 77

Cropper, M., Katz, D., Sartoretti, P., et al. 2018, A&A, 616, A5

Crouzet, N., Chapellier, E., Guillot, T., et al. 2018, A&A, 619, A116

Curtis, J. L., Agüeros, M. A., Douglas, S. T., & Meibom, S. 2019a, ApJ, 879, 49

Curtis, J. L., Agüeros, M. A., Mamajek, E. E., Wright, J. T., & Cummings, J. D. 2019b, AJ, 158, 77

Daban, J.-B., Gouvret, C., Guillot, T., et al. 2010, 7733, 77334T

Damiani, F., Prisinzano, L., Pillitteri, I., Micela, G., & Sciortino, S. 2019, Astronomy & Astrophysics, 623, A112, publisher: EDP Sciences

Dauphas, N., & Pourmand, A. 2011, Nature, 473, 489

David, T., Hillenbrand, L., & Petigura, E. 2016, Nature, 534, 658

David, T. J., & Hillenbrand, L. A. 2015, ApJ, 804, 146

David, T. J., Petigura, E. A., Luger, R., et al. 2019a, ApJL, 885, L12

David, T. J., Mamajek, E. E., Vanderburg, A., et al. 2018, AJ, 156, 302

David, T. J., Cody, A. M., Hedges, C. L., et al. 2019b, AJ, 158, 79

de Zeeuw, P. T., Hoogerwerf, R., de Bruijne, J. H. J., Brown, A. G. A., & Blaauw, A. 1999, AJ, 117, 354

Dobbie, P. D., Lodieu, N., & Sharp, R. G. 2010, MNRAS, 409, 1002

Donati, J.-F., Semel, M., Carter, B. D., Rees, D. E., & Collier Cameron, A. 1997, MNRAS, 291, 658

Donati, J. F., Moutou, C., Malo, L., et al. 2016, Nature, advance online publication

Dotter, A. 2016, ApJS, 222, 8

Douglas, S. T., Agüeros, M. A., Covey, K. R., & Kraus, A. 2017, ApJ, 842, 83

Douglas, S. T., Curtis, J. L., Agüeros, M. A., et al. 2019, ApJ, 879, 100

Dullemond, C. P., & Monnier, J. D. 2010, ARA&A, 48, 205

Díaz, R. F., Almenara, J. M., Santerne, A., et al. 2014, MNRAS, 441, 983
Ekström, S., Georgy, C., Eggenberger, P., et al. 2012, A&A, 537, A146
Evans, D. W., Riello, M., De Angeli, F., et al. 2018, A&A, 616, A4
Fabrycky, D., & Tremaine, S. 2007, ApJ, 669, 1298
Fedele, D., van den Ancker, M. E., Henning, T., Jayawardhana, R., & Oliveira, J. M. 2010, Astronomy and Astrophysics, 510, A72
Feiden, G. A., & Chaboyer, B. 2013, ApJ, 779, 183
Fűrész, G., Szentgyorgyi, A. H., & Meibom, S. 2008, 287
Flagg, L., Johns-Krull, C. M., Nofi, L., et al. 2019, ApJ, 878, L37
Foreman-Mackey, D. 2016, The Journal of Open Source Software, 24
Foreman-Mackey, D., Czekala, I., Luger, R., et al. 2020, exoplanet-dev/exoplanet v0.2.6
Fortney, J. J., Marley, M. S., & Barnes, J. W. 2007, ApJ, 659, 1661
Fulton, B. J., Petigura, E. A., Blunt, S., & Sinukoff, E. 2018, PASP, 130, 044504
Fulton, B. J., Petigura, E. A., Howard, A. W., et al. 2017, AJ, 154, 109
Gaia Collaboration, Prusti, T., de Bruijne, J. H. J., et al. 2016, A&A, 595, A1
Gaia Collaboration, Brown, A. G. A., Vallenari, A., et al. 2018, A&A, 616, A1
Gaudi, B. S., & Winn, J. N. 2007, ApJ, 655, 550
Gelman, A., & Rubin, D. B. 1992, Statistical Science, 7, 457, publisher: Institute of Mathematical Statistics
Giacalone, S., & Dressing, C. D. 2020, arXiv e-prints, arXiv:2002.00691
Gilbert, J., Bergmann, C., Bloxham, G., et al. 2018, 0702, 107020Y, Conference Name: Ground-based and Airborne Instrumentation for Astronomy VII ISBN: 9781510619579 Place: eprint: arXiv:1807.01938
Ginsburg, A., Sipocz, B., Madhura Parikh, et al. 2018, Astropy/Astroquery: V0.3.7 Release
Girardi, L., Groenewegen, M. A. T., Hatziminaoglou, E., & da Costa, L. 2005, A&A, 436, 895
Gray, D. F. 2005, The Observation and Analysis of Stellar Photospheres
Gray, R. O., & Corbally, C. J. 1994, AJ, 107, 742
Gupta, A., & Schlichting, H. E. 2019, MNRAS, 487, 24
—. 2020, MNRAS, 493, 792
Hartman, J. D., Gaudi, B. S., Holman, M. J., et al. 2009, ApJ, 695, 336
Hippke, M., David, T. J., Mulders, G. D., & Heller, R. 2019, arXiv:1906.00966 [astro-ph], arXiv: 1906.00966
Hirano, T., Krishnamurthy, V., Gaidos, E., et al. 2020, arXiv:2006.13243 [astro-ph], arXiv: 2006.13243
Hoffman, M. D., & Gelman, A. 2014, Journal of Machine Learning Research, 15, 1593
Howard, A. W., Marcy, G. W., Bryson, S. T., et al. 2012, ApJS, 201, 15
Howell, S. B., Sobeck, C., Haas, M., et al. 2014, PASP, 126, 398
Huang, C. X., Shporer, A., Dragomir, D., et al. 2018a, arXiv:1807.11129 [astro-ph], arXiv: 1807.11129
Huang, C. X., Burt, J., Vanderburg, A., et al. 2018b, ApJ, 868, L39
Hunter, J. D. 2007, Computing in Science & Engineering, 9, 90
Irwin, J., & Bouvier, J. 2009, in , eprint: arXiv:0901.3342, 363
Irwin, J., Irwin, M., Aigrain, S., et al. 2007, MNRAS, 375, 1449
Jenkins, J. M., Twicken, J. D., McCauliff, S., et al. 2016, Software and Cyberinfrastructure for Astronomy IV, 9913, 99133E
Jensen, E. 2013, Tapir: A web interface for transit/eclipse observability, Astrophysics Source Code Library, ascl:1306.007
Johns-Krull, C. M., McLane, J. N., Prato, L., et al. 2016, ApJ, 826, 206
Jones, E., Oliphant, T., Peterson, P., et al. 2001, Open source scientific tools for Python
Jordán, A., Brahm, R., Espinoza, N., et al. 2020, AJ, 159, 145
Kaufer, A., Stahl, O., Tubbesing, S., et al. 1999, The Messenger, 95, 8
Kharchenko, N. V., Piskunov, A. E., Röser, S., Schilbach, E., & Scholz, R.-D. 2005, A&A, 438, 1163
Kharchenko, N. V., Piskunov, A. E., Schilbach, E., Röser, S., & Scholz, R.-D. 2013, A&A, 558, A53
Kipping, D. M. 2013, MNRAS, 435, 2152
Kleine, T., Touboul, M., Bourdon, B., et al. 2009, Geochimica et Cosmochimica Acta, 73, 5150
Kounkel, M., & Covey, K. 2019, AJ, 158, 122
Krumholz, M. R., McKee, C. F., & Bland-Hawthorn, J. 2019, ARA&A, 57, 227
Kurucz, R. L. 2013, Astrophysics Source Code Library, ascl:1303.024
König, S., Münker, C., Hohl, S., et al. 2011, Geochimica et Cosmochimica Acta, 75, 2119
Lada, C. J., & Lada, E. A. 2003, ARA&A, 41, 57
Landsman, W. B. 1995, in Astronomical Society of the Pacific Conference Series, Vol. 77, Astronomical Data Analysis Software and Systems IV, ed. R. A. Shaw, H. E. Payne, & J. J. E. Hayes, 437
Lightkurve Collaboration, Cardoso, J. V. d. M., Hedges, C., et al. 2018, Lightkurve: Kepler and TESS time series analysis in Python, Astrophysics Source Code Library, ascl:1812.013
Lin, D. N. C., Bodenheimer, P., & Richardson, D. C. 1996, Nature, 380, 606
Lindegren, L., Hernández, J., Bombrun, A., et al. 2018, Astronomy & Astrophysics, 616, A2
Lithwick, Y., & Wu, Y. 2014, Proceedings of the National Academy of Sciences, 111, 12610
Livingston, J. H., Dai, F., Hirano, T., et al. 2018, AJ, 155, 115

—. 2019, MNRAS, 484, 8
Lomb, N. R. 1976, Astrophysics and Space Science, 39, 447
Lovis, C., & Mayor, M. 2007, A&A, 472, 657
Luger, R., Agol, E., Foreman-Mackey, D., et al. 2019, AJ, 157, 64
Malavolta, L., Nascimbeni, V., Piotto, G., et al. 2016, A&A, 588, A118
Mamajek, E. E. 2009, 1158, 3, Conference Name: Exoplanets and Disks: Their Formation and Diversity Place: eprint: arXiv:0906.5011
Mamajek, E. E., & Hillenbrand, L. A. 2008, ApJ, 687, 1264
Mann, A. W., Gaidos, E., & Ansdell, M. 2013, The Astrophysical Journal, 779, 188
Mann, A. W., Gaidos, E., Mace, G. N., et al. 2016a, ApJ, 818
Mann, A. W., Newton, E. R., Rizzuto, A. C., et al. 2016b, AJ, 152, 61
Mann, A. W., Gaidos, E., Vanderburg, A., et al. 2017, AJ, 153, 64
Mann, A. W., Vanderburg, A., Rizzuto, A. C., et al. 2018, AJ, 155, 4
Mann, A. W., Johnson, M. C., Vanderburg, A., et al. 2020, arXiv:2005.00047 [astro-ph], arXiv: 2005.00047
Mansfield, M., Bean, J. L., Oklopčić, A., et al. 2018, ApJ, 868, L34, arXiv: 1812.02214
Martioli, E., Hebrard, G., Moutou, C., et al. 2020, arXiv:2006.13269 [astro-ph], arXiv: 2006.13269
Mayor, M., Marmier, M., Lovis, C., et al. 2011, ArXiv e-prints, 1109, arXiv:1109.2497
McKinney, W. 2010, in Proceedings of the 9th Python in Science Conference, ed. S. van der Walt & J. Millman, 51
Meibom, S., Barnes, S. A., Platais, I., et al. 2015, Nature, 517, 589
Meibom, S., Torres, G., Fressin, F., et al. 2013, Nature, 499, 55
Mékarnia, D., Guillot, T., Rivet, J.-P., et al. 2016, MNRAS, 463, 45
Mermilliod, J. C. 1981, A&A, 97, 235
Miller, A. A., Irwin, J., Aigrain, S., Hodgkin, S., & Hebb, L. 2008, MNRAS, 387, 349
Mochejska, B. J., Stanek, K. Z., Sasselov, D. D., et al. 2005, AJ, 129, 2856
—. 2006, AJ, 131, 1090
Montet, B. T., Feinstein, A. D., Luger, R., et al. 2019, arXiv:1912.03794 [astro-ph], arXiv: 1912.03794
Morbidelli, A., Lunine, J. I., O'Brien, D. P., Raymond, S. N., & Walsh, K. J. 2012, Annual Review of Earth and Planetary Sciences, 40, 251
Morton, T. D. 2012, ApJ, 761, 6
Morton, T. D. 2015a, isochrones: Stellar model grid package
—. 2015b, VESPA: False positive probabilities calculator, Astrophysics Source Code Library, ascl:1503.011
Morton, T. D., Bryson, S. T., Coughlin, J. L., et al. 2016, ApJ, 822, 86, arXiv: 1605.02825
Netopil, M., Paunzen, E., Heiter, U., & Soubiran, C. 2016, A&A, 585, A150
Newton, E. R., Mann, A. W., Tofflemire, B. M., et al. 2019, ApJ, 880, L17
Obermeier, C., Henning, T., Schlieder, J. E., et al. 2016, AJ, 152, 223
Oh, S., Price-Whelan, A. M., Hogg, D. W., Morton, T. D., & Spergel, D. N. 2017, AJ, 153, 257
Oklopčić, A., & Hirata, C. M. 2018, ApJL, 855, L11
Owen, J. E., & Wu, Y. 2013, ApJ, 775, 105
Palle, E., Oshagh, M., Casasayas-Barris, N., et al. 2020, arXiv:2006.13609 [astro-ph], arXiv: 2006.13609
Paxton, B., Bildsten, L., Dotter, A., et al. 2011, ApJS, 192, 3
Paxton, B., Cantiello, M., Arras, P., et al. 2013, ApJS, 208, 4
Paxton, B., Marchant, P., Schwab, J., et al. 2015, ApJS, 220, 15
Pepper, J., Stanek, K. Z., Pogge, R. W., et al. 2008, AJ, 135, 907
Pérez, F., & Granger, B. E. 2007, Computing in Science and Engineering, 9, 21
Petigura, E. A., Marcy, G. W., Winn, J. N., et al. 2018, AJ, 155, 89
Plavchan, P., Barclay, T., Gagné, J., et al. 2020, Nature, 582, 497, arXiv: 2006.13248
Pollack, J. B., Hubickyj, O., Bodenheimer, P., et al. 1996, Icarus, 124, 62
Quinn, S. N., White, R. J., Latham, D. W., et al. 2012, ApJL, 756, L33
Raghavan, D., McAlister, H. A., Henry, T. J., et al. 2010, ApJS, 190, 1, arXiv: 1007.0414
Rajpaul, V., Aigrain, S., Osborne, M. A., Reece, S., & Roberts, S. 2015, Monthly Notices of the Royal Astronomical Society, 452, 2269
Rajpurohit, A. S., Reylé, C., Allard, F., et al. 2013, Astronomy and Astrophysics, 556, A15
Randich, S., Tognelli, E., Jackson, R., et al. 2018, Astronomy & Astrophysics, 612, A99
Raymond, S. N., Kokubo, E., Morbidelli, A., Morishima, R., & Walsh, K. J. 2014, Protostars and Planets VI, 595
Rebull, L. M., Stauffer, J. R., Cody, A. M., et al. 2020
Rebull, L. M., Stauffer, J. R., Bouvier, J., et al. 2016, AJ, 152, 113
Ricker, G. R., Winn, J. N., Vanderspek, R., et al. 2015, Journal of Astronomical Telescopes, Instruments, and Systems, 1, 014003
Rizzuto, A. C., Vanderburg, A., Mann, A. W., et al. 2018, arXiv:1808.07068 [astro-ph], arXiv: 1808.07068
Rizzuto, A. C., Newton, E. R., Mann, A. W., et al. 2020, arXiv:2005.00013 [astro-ph], arXiv: 2005.00013
Rohatgi, A. 2019, WebPlotDigitizer: v4.2
Salvatier, J., Wieckiâ, T. V., & Fonnesbeck, C. 2016, PyMC3: Python probabilistic programming framework
Santerne, A., Díaz, R. F., Almenara, J.-M., et al. 2015, MNRAS, 451, 2337
Sato, B., Izumiura, H., Toyota, E., et al. 2007, ApJ, 661, 527
Scargle, J. D. 1982, ApJ, 263, 835
Seager, S., & Mallén-Ornelas, G. 2003, ApJ, 585, 1038

Servén, D., Brummitt, C., & Abedi, H. 2018, dswah/pyGAM: v0.8.0
Skrutskie, M. F., Cutri, R. M., Stiening, R., et al. 2006, AJ, 131, 1163
Skumanich, A. 1972, ApJ, 171, 565
Smith, J. C., Morris, R. L., Jenkins, J. M., et al. 2016, PASP, 128, 124501
Smith, J. C., Stumpe, M. C., Cleve, J. E. V., et al. 2012, PASP, 124, 1000
Soderblom, D. R. 2010, ARA&A, 48, 581
Soderblom, D. R., Hillenbrand, L. A., Jeffries, R. D., Mamajek, E. E., & Naylor, T. 2014, Protostars and Planets VI, 219
Spake, J. J., Sing, D. K., Evans, T. M., et al. 2018, Nature, 557, 68, arXiv: 1805.01298
Stassun, K. G., Collins, K. A., & Gaudi, B. S. 2017, AJ, 153, 136
Stassun, K. G., Oelkers, R. J., Pepper, J., et al. 2018, AJ, 156, 102
Stassun, K. G., Oelkers, R. J., Paegert, M., et al. 2019, arXiv:1905.10694 [astro-ph], arXiv: 1905.10694
Stauffer, J. R., Hartmann, L. W., Prosser, C. F., et al. 1997, ApJ, 479, 776
Stauffer, J. R., Jones, B. F., Backman, D., et al. 2003, AJ, 126, 833
Stumpe, M. C., Smith, J. C., Catanzarite, J. H., et al. 2014, PASP, 126, 100
Sullivan, P. W., et al. 2015, ApJ, 809, 77
Theano Development Team. 2016, arXiv e-prints, abs/1605.02688
Tokovinin, A. 2018, PASP, 130, 035002, arXiv: 1801.04772
Tokovinin, A., Fischer, D. A., Bonati, M., et al. 2013, PASP, 125, 1336
Torres, G., Fressin, F., Batalha, N. M., et al. 2011, ApJ, 727, 24
van Leeuwen, F. 2009, A&A, 497, 209
Vanderburg, A., Mann, A. W., Rizzuto, A., et al. 2018, arXiv:1805.11117 [astro-ph], arXiv: 1805.11117
Vanderburg, A., Huang, C. X., Rodriguez, J. E., et al. 2019, ApJ, 881, L19
VanderPlas, J. T., & Ivezić, Z. 2015, ApJ, 812, 18
Walt, S. v. d., Colbert, S. C., & Varoquaux, G. 2011, Computing in Science & Engineering, 13, 22
Weber, E. J., & Davis, Jr., L. 1967, ApJ, 148, 217
Williams, J. P., & Cieza, L. A. 2011, ARA&A, 49, 67
Wright, E. L., Eisenhardt, P. R. M., Mainzer, A. K., et al. 2010, AJ, 140, 1868
Wright, J. T., Marcy, G. W., Howard, A. W., et al. 2012, ApJ, 753, 160
Yu, L., Donati, J.-F., Hébrard, E. M., et al. 2017, Monthly Notices of the Royal Astronomical Society, 467, 1342
Zahn, J.-P. 1977, A&A, 500, 121
Zhou, G., Rodriguez, J. E., Vanderburg, A., et al. 2018, AJ, 156, 93
Zhou, G., Winn, J. N., Newton, E. R., et al. 2019, arXiv:1912.04095 [astro-ph], arXiv: 1912.04095
Ziegler, C., Tokovinin, A., Briceño, C., et al. 2020, AJ, 159, 19
Zuckerman, B., & Song, I. 2004, ARA&A, 42, 685
Žerjal, M., Zwitter, T., Matijevič, G., et al. 2017, ApJ, 835, 61
Žerjal, M., Ireland, M. J., Nordlander, T., et al. 2019, MNRAS, 484, 4591